Author's Accepted Manuscript

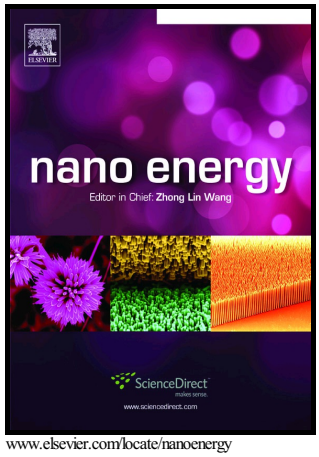

www.elsevier.com/locate/nanoenergy

A Comprehensive Review of Flexible Piezoelectric Generators Based on Organic-Inorganic Metal Halide Perovskites

Venkatraju Jella, Swathi Ippili, Ji-Ho Eom, S.V.N. Pammi, Jang-Soo Jung, Van-Dang Tran, Van Hieu Nguyen, Artavazd Kirakosyan, Seokjin Yun, Deul Kim, Moon Ryul Sihn, Jihoon Choi, Yun-Jeong Kim, Hye-Jin Kim, Soon-Gil Yoon

PII: S2211-2855(18)30943-1
DOI: https://doi.org/10.1016/j.nanoen.2018.12.038
Reference: NANOEN3286

To appear in: *Nano Energy*

Received date: 30 September 2018
Revised date: 28 November 2018
Accepted date: 10 December 2018

Cite this article as: Venkatraju Jella, Swathi Ippili, Ji-Ho Eom, S.V.N. Pammi, Jang-Soo Jung, Van-Dang Tran, Van Hieu Nguyen, Artavazd Kirakosyan, Seokjin Yun, Deul Kim, Moon Ryul Sihn, Jihoon Choi, Yun-Jeong Kim, Hye-Jin Kim and Soon-Gil Yoon, A Comprehensive Review of Flexible Piezoelectric Generators Based on Organic-Inorganic Metal Halide Perovskites, *Nano Energy,* https://doi.org/10.1016/j.nanoen.2018.12.038

This is a PDF file of an unedited manuscript that has been accepted for publication. As a service to our customers we are providing this early version of the manuscript. The manuscript will undergo copyediting, typesetting, and review of the resulting galley proof before it is published in its final citable form. Please note that during the production process errors may be discovered which could affect the content, and all legal disclaimers that apply to the journal pertain.

ACCEPTED MANUSCRIPT

A Comprehensive Review of Flexible Piezoelectric Generators Based on Organic-Inorganic Metal Halide Perovskites

Venkatraju Jella[1], Swathi Ippili[1], Ji-Ho Eom[1], S. V. N. Pammi[1], Jang-Soo Jung[1], Van-Dang Tran[1], Van Hieu Nguyen[2], Artavazd Kirakosyan[1], Seokjin Yun[1], Deul Kim[1], Moon Ryul Sihn[1], Jihoon Choi[1,*], Yun-Jeong Kim[3], Hye-Jin Kim[3,*], Soon-Gil Yoon[1,*]

[1]Department of Materials Science and Engineering, Chungnam National University, Daeduk Science Town, 34134, Daejeon, Republic of Korea

[2]Nanosensors group, Faculty of Electrical and Electronic Engineering, Phenikaa University, Yen Nghia, Ha-Dong District, Hanoi 1000, Viet Nam

[3]Multidisciplinary Sensor Research Group, Electronics and Telecommunication Research Institute, 34129, Daejeon, Republic of Korea

[ξ]Both authors contributed equally to this work

jihoonc@cnu.ac.kr

nolawara@etri.re.kr

sgyoon@cnu.ac.kr

[*]Corresponding author:

Accepted manuscript

Abstract

Organic-inorganic metal halide perovskites (OMHPs) have been extensively investigated over the past few years, not only because of their key features such as ease of solution-based processing, strong optical absorption, tunable bandgap, high carrier mobility, a long diffusion length, etc., and also because of their multi-faceted electronic applications with unprecedented power conversions efficiencies (PCE) in the field of photovoltaics. Apart from the impressive photovoltaic and optoelectronic applications, the applications for OMHPs have recently diverged

ACCEPTED MANUSCRIPT

towards mechanical energy harvesting applications owing to high levels of dielectric and piezoelectric properties that are relatively analogous to those of inorganic piezoelectric materials. Despite these assets, a fundamental understanding of physical behaviors such as ferroelectric and piezoelectric properties remains a key challenge that hampers the development of OMHP-based piezoelectric energy harvesters. This review updates the progress in nanogenerators for mechanical energy harvesting based on OMHPs and includes materials classifications and structural properties, as well as an overview of dielectric, ferroelectric, and piezoelectric properties based on the available literature. In addition, the numerous methods used to synthesize high-quality perovskite films and crystals are also addressed. In the overview of piezoelectric generators (PEGs), various approaches to PEGs based on OMHPs and flexible polymer composites are introduced. For flexible PEGs, fabrication, structural design, factors determining output, and applications are reviewed. Finally, some essential experimental features, perspectives, and issues in this exciting field are discussed and suggested.

Accepted manuscript

Graphical Abstract

This review article summarizes the recent development of flexible piezoelectric nanogenerators based on organic-inorganic metal halide perovskite (OMHP) materials and their polymer composites. Dielectric, ferroelectric and piezoelectric properties of OMHPs are also discussed in detail.

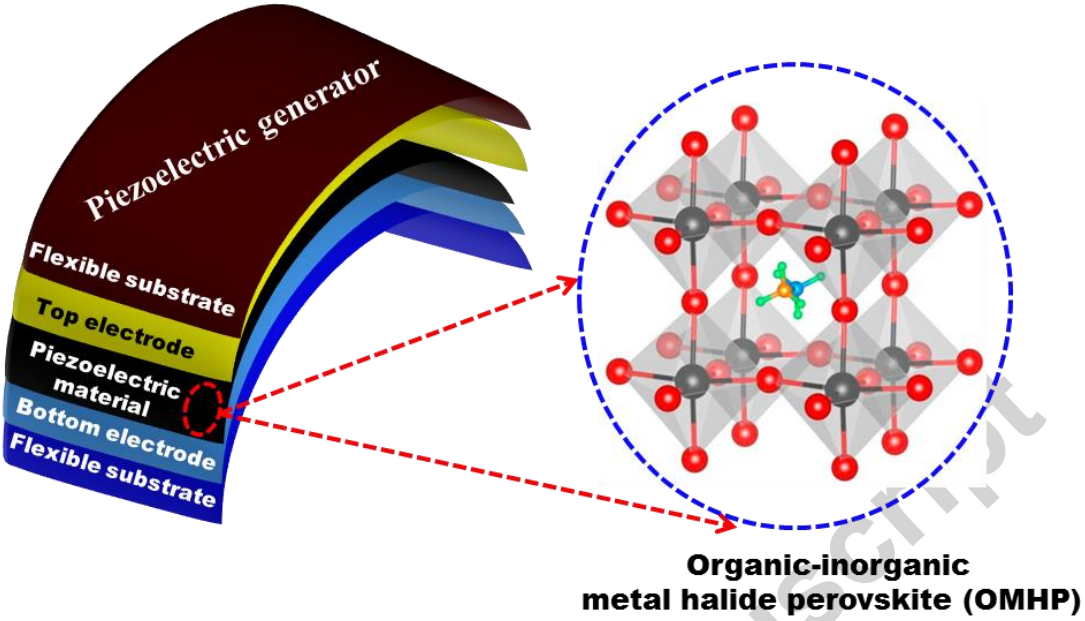

Keywords: Organic-inorganic metal halide perovskite, Piezoelectric properties, OMHP-polymer composite based piezoelectric generator, Flexibility

Accepted manuscript

1. Introduction

Given the depletion of fossil energy resources and growing energy demands, the development of sources of alternative sustainable energy has become imperative for sustainable economic growth. Even though many forms of natural energy sources such as solar, hydro, and wind power can alleviate energy demands, these are greatly affected by environmental factors and are impractical for indoor operations. Thus, energy scavenging from environmentally abundant

ACCEPTED MANUSCRIPT

forms of wasted mechanical energy such as human motion, biomechanical, walking, jogging, wind, water flow, vibrations, etc., is promising approach that could be used to develop renewable, portable and sustainable energy [1-5]. Various approaches have been established to harvest abundant mechanical energy into usable electricity via various mechanisms such as the piezoelectric effect, electromagnetic induction, and electrostatic generation [6-8]. Among these, piezoelectric generators (PEGs) have attracted intensive attention owing to a capability for direct power conversion and relatively easier manufacturing [9-12]. Numerous PEGs with different structures and functions have been developed for efficient power conversion based on various types of piezoelectric materials including semiconductors [13-16], ceramic materials [17-20] and poly (vinylidene fluoride) (PVDF) [21] and its copolymers [22]). Traditionally, ceramic perovskite materials (PZT) are potential candidates for piezoelectric applications due to high dielectric and piezoelectric properties that are ideal for the conversion of mechanical energy to electricity [23-25]. Despite their high level of output voltage generation, the complicated fabrication process, high-temperature calcination, brittle and rigid nature of inorganic perovskites make it difficult to integrate with soft materials that can render the devices impractical for wider applications [26-28]. Therefore, many piezoelectric materials, which can be synthesized *via* cost-effective and low-temperature synthesis processes, still require investigation in order to realize highly flexible, durable, and stretchable PEGs with high performance for large-scale applications.

In recent years, OMHPs have drawn a remarkable level of attention from photovoltaic researchers because of numerous outstanding optical and electrical properties that offer the advantages of inexpensive and low-temperature solution-processed fabrication [29-31]. Perovskite materials are considered as most promising candidates for next-generation cost-

Accepted manuscript

ACCEPTED MANUSCRIPT

effective solar cells that are highly efficient owing to an unprecedented rise in power conversion efficiency of more than 22% [32]. Despite this rapid and impressive progress in the perovskite solar cell field, these materials continue to trigger the development of a wide range of other applications such as light-emitting diodes (LEDs), photo detectors, thin film transistors (TFT), sensors, resistive random-axis memory (ReRAM), piezoelectric devices and so on [33-39]. Among these, piezoelectric devices based on OMHPs have garnered the most interest due to intriguing piezo/ferroelectric properties. OMHP materials exhibit structural phase transition that is similar to other inorganic perovskite materials leading to ferroelectric polarization [40]. Kutes et al. experimentally observed ferroelectric domains in solution-processed β-$MAPbI_3$ thin films using piezoforce microscopy (PFM) [41]. Furthermore, many researchers have investigated the piezoelectric properties of OMHP films, which can be enhanced under illumination [42,43]. In particular, $MAPbI_3$ perovskite revealed a high piezoelectric coefficient of ~ 25 pm/V under illumination [42]. Various OMHP-based PEGs with different structures and functions have also been developed for mechanical energy harvesting [39,44,45]. However, OMHPs have a brittle and inflexible nature similar to inorganic perovskite materials, which is a major concern for stretchable/flexible device applications. Many researchers have focused on developing high-performance, flexible generators *via* blending with polymers using a simple solution process. However, the use of OMHPs in piezoelectric device applications is a relatively recent development and further study is required to broaden their practical applications.

Even though OMHPs are widely used in photovoltaic applications, we limited this comprehensive review to piezoelectric energy harvesters that are based on OMHPs. This review focuses on the recent progress of OMHPs and associated polymer composites that are being used for the development of piezoelectric energy harvesting applications that include flexible PEGs.

Accepted manuscript

ACCEPTED MANUSCRIPT

We briefly review recent theoretical and experimental investigations on the dielectric, piezoelectric and ferroelectric properties of OMHP materials followed by various synthesis routes that are used to obtain high-quality perovskite materials. Finally, we present a brief outlook into the problems, current challenges, and future prospects for OMHP-based nanogenerators.

2. Crystal structure and electrical properties of organic-inorganic metal halide perovskite

2.1. Crystal structure

Perovskites are inorganic crystals with ABX_3 structure that have the same crystalline structure as calcium titanate ($CaTiO_3$) [46]. Although most perovskite materials are oxides, OMHPs are the focus of the present study. OMHPs have the general formula ABX_3 (A = organic monovalent cation, B = divalent metal cation and X = halide anion, respectively), as shown in Figure 1a [47]. The cations A and B are coordinated with 12 and 6 X anions that form cuboctahedral and octahedral geometries, respectively. The structural formability and stability of the ABX_3 perovskite crystals are evaluated by their geometrical tolerance factor (t) [48] and by an octahedral factor (μ) [49], $t= (R_A+R_X)/(\sqrt{2}(R_B+R_X)$, where R_A, R_B and R_X are the effective ionic radii for A, B and X ions, respectively. The ratio of R_B/R_X is defined as μ, which directly correlates with a BX_6 octahedron. For OMHP materials, the expected formability and octahedral factors are in the ranges of $0.813 < t < 1.107$ [50, 51] and $0.44 < \mu < 0.90$ [52], respectively. OMHPs tend to form cubic structures when $0.8 < t < 1.0$, an orthorhombic structure if $t < 0.8$, and hexagonal if $t > 1$ [53,54]. The most commonly used organic cations are methylammonium ($MA^+ = CH_3NH_3^+$, R_A = 1.8 Aº) [55] and formamidinium ($FA^+ = CH(NH_2)_2^+$, R_A = 2.7 Aº) [55, 56], while inorganic divalent cations are Pb (R_B = 1.19 Aº) and Sn (1.10 Aº). The anion X

ACCEPTED MANUSCRIPT

dictates halogens such as Cl (R_x = 1.18 Aº), Br (R_x = 1.96 Aº), and I (R_x = 2.2 Aº). The correlation of the calculated tolerance factor-octahedral factor (t-μ) for commonly employed perovskites is depicted in Figure 1b [57]. The calculated tolerance factors for $MAPbX_3$ (X = Cl, Br, I) are $0.84 < t < 0.85$. The calculated tolerance factor for $MAPbI_3$ is 0.83, which deviates from the expected ideal cubic structure. However, other non-geometric factors such as the ionization energy of organic-inorganic cations [58] as well as chemical stability and valence band [59] also significantly influence the structure formability and the stability of ABX_3 perovskites.

An interesting feature of perovskite materials is that structural phase transition depends on a dynamic tilting of the octahedra in the lattice [60]. In the case of $MAPbI_3$, MA^+ cation resides within the inorganic framework of corner sharing PbI_6 octahedra, which has different tilting characteristics for the differing orthorhombic, tetragonal and cubic structures. Based on XRD analysis, $MAPbI_3$ reveals tetragonal-to-cubic and tetragonal-to-orthorhombic structural transition at temperatures of 330 and 170 K, respectively, [61,62]. In addition, replacement of Pb^{2+} with a various other metal cations as well as partial substitution of iodine with Cl and Br in $MAPbI_3$ modifies the crystal structure at room temperature [44,63-68]. Moreover, partial replacement of FA^+ with MA^+ or Pb^{2+} with environmentally favored Sn^{2+} in $FAPbI_3$ perovskite enhances the stability of the α-phase of FA-based perovskites [69]. In addition to lead-based OMHPs, lead-free tin-based perovskites are other promising materials for photovoltaic applications, with the noted exception of stability factors [70]. Tin-based perovskites are prone to oxidize rapidly upon exposure to ambient conditions, which makes them inappropriate for many applications [40,71]. Ju et al. reported the attainment of stability for Sn-based perovskites by partially doping Sn with Pb under air ambient conditions [72]. Therefore, the stoichiometric fine-tuning of ABX_3 allows

Accepted manuscript

ACCEPTED MANUSCRIPT

the design of various functional perovskites with a wide range of the structural, optical, electrical, and magnetic properties [73].

2.2. Dielectric properties

A dielectric is a non-conducting substance that can be polarized under the influence of an applied electric field. The response of a material to an applied electric field is defined by its conductivity and permittivity. Dielectric permittivity of the material is the sum of the real and imaginary parts of complex dielectric constants under alternate current (ac) conditions, as depicted in the following equation.

$$\varepsilon_r = \varepsilon_r' - j\varepsilon_r''$$

In this equation, ε_r' is the real part, which can be defined as the ability of the material to store energy; ε_r'' is the imaginary part, which is also referred to as the loss factor; and, j represents imaginary constant values to $\sqrt{-1}$. However, in dielectric materials there are various polarization mechanisms such as electronic, ionic, rotational or dipolar, and space charge or interfacial. Moreover, each of these types of polarization requires a certain amount of time to perform, which results in a frequency dependency for polarization and a dielectric permittivity, as clearly depicted in Figure 2 [74].

Similar to inorganic perovskite materials, the presence of a polar molecule (organic cation) at the center of a crystal structure intriguingly introduces the possibility of orientational disorder and polarization in OMHPs [75]. The organic cations ($CH_3NH_3^+$ ion) have a permanent electric dipole moment, and the orientations of these ions significantly contribute to the dielectric properties of perovskites [64,76,77]. Theoretical and experimental studies of the dielectric properties of OMHPs have been conducted by several research groups [78-85]. In 1887,

Accepted manuscript

ACCEPTED MANUSCRIPT

Poglitsch and Weber performed the first temperature-dependent dielectric measurements of $MAPbX_3$ (X=Cl, Br, I) perovskites, which revealed the discontinuity in dielectric constants during transition from the orthorhombic phase to the tetragonal phase [64]. Based on frequency and temperature dependent dielectric studies, Onoda-Yamamuro et al. reported that the increasing hindrance of the motion of MA^+ cations upon cooling, resulted in a slower response time and larger dielectric constants at orthorhombic-tetragonal phase transition for $MAPbX_3$ (X = Cl, Br, I) perovskites [86]. Ever since many research groups have conducted dielectric studies on OMHPs to understand the structural changes and optical properties of OMHPs in order to model and design highly efficient photovoltaic devices [87-92].

Recently, Govinda et al. reported both $MAPbBr_3$ and $MAPbI_3$ undergo a tetragonal-orthorhombic phase transition by lowering the temperature, indicating that the dipoles on MA^+ units behave like free dipoles that contribute prominently to dielectric values [93]. The $MAPbI_3$ exhibits phase-transition temperature of 162 K for all measured frequencies, as shown in Figure 3a. Furthermore, Kim et al. demonstrated that $MAPbI_3$ thin films exhibit tetragonal-cubic phase transition with increases in temperature, which has been confirmed by dielectric studies measured at 100 kHz, as shown in Figure 3b [39]. In addition, the dielectric response of $MAPbI_3$ is notably influenced by light illumination, which is increased rapidly from ~ 10^3 (dark) to ~ 10^6 under one sun illumination at lower frequencies due to contributions from electronic carriers [94]. Moreover, the dielectric discrepancies of $MAPbI_3$ films were observed by incorporating partial amounts of Fe^{2+} into $MAPbI_3$ [44]. As shown in Figure 3c, the dielectric constant (ε_r) at 100 kHz is remarkably increased with increases in Fe^{2+} content, but then displays a quick decline with greater Fe^{2+} indicating a ferroelectric-paraelectric transition of $MAPb_{1-x}Fe_xI_3$ films with an Fe^{2+} content of x = 0.10. Similarly, OMHPs with the structures of (3-pyrrolinium)($CdCl_3$),

Accepted manuscript

ACCEPTED MANUSCRIPT

(benzylammonium)$_2PbCl_4$, $Me_3NCH_2ClMnCl_3$ (TMCM-$MnCl_3$), and TMCM-$CdCl_3$, and Me_2NH_2-PbI_3 ($DMAPbI_3$) reveal high dielectric properties and exhibit similar dielectric behavior of phase transitions near curie-temperature (T_c) [95-98]. These results showed that tuning of the OMHP functional materials resulted in an enhancement in the dielectric and piezoelectric properties.

In addition to the dielectric properties of OMHPs, researchers have focused on investigating the dielectric response in OMHP-polymer composite films, which is essential to understanding the piezoelectricity in composite-based films [99,100]. In principle, heterogeneous materials interface in composite films cause an interfacial, or Maxwell-Wagner-Sillars (MWS), polarization, which induces an abrupt change in the total dielectric constant [101-103]. When the concentration or distribution of nanoparticles increases in film, the distance between OMHP nanoparticles becomes narrow and solidified, which results in larger dipole polarization. Solidified cations lead to rapid increases in the dielectric constant and polarization, which is clear in the dielectric measurements of $MAPbI_3$-PVDF composite films, as shown in Figure 3d [100]. Thus, the increase in the dielectric constant will lead to an increased piezoelectric constant, which is similar to that seen in PZT-PVDF composites [104-106].

2.3. Ferroelectric properties

Ferroelectric materials are dielectric materials with the ability to alter the direction of their spontaneous polarization in accordance with an applied electric field, where the spontaneous polarization originates from a non-centrosymmetric structure. Ferroelectric materials with ABO_3 crystal structures exhibit unique properties such as spontaneous polarization, polarization reversal, and ferroelectric-to-paraelectric phase transition at Curie temperature (T_c). Spontaneous

Accepted manuscript

ACCEPTED MANUSCRIPT

polarization arises from the breaking of the crystal centrosymmetry as a result of BX_6 octahedron distortion, which originates when the B cation moves away from the center of the BX_6 octahedron [60]. Recently, the structural transitions and enormous dielectric properties of OMHPs have allowed investigations into the ferroelectric properties in order to understand the current-voltage hysteresis in OMHP-based photovoltaics [107]. In particular, $MAPbI_3$ exhibits spontaneous polarization due to the presence of MA^+ cations, and its reorientation leads to a distortion of the PbI_6 by decreasing the crystal lattice symmetry [76]. Frost et al. theoretically calculated and proposed the existence of ferroelectric domains in OMHPs, which result in internal junctions that may aid in the separation of photoexcited charge carriers and a reduced recombination rate in perovskite solar cells [76]. Zheng et al. demonstrated the bulk ferroelectric properties of $MAPbI_3$ and $MAPbI_{3-x}Cl_x$ using first-principle calculations. When the net dipole moments of MA^+ molecules are aligned along the c-axis in a tetragonal structure, $MAPbI_3$ reveals a polarization of 6.8 $\mu C/cm^2$, whereas Cl substitution in $MAPbI_3$ has no substantial effect on polarization [108].

Although theoretical studies have paved the way to investigate the ferroelectric properties of OMHPs, experimental observations are necessary to verify authenticity. Stoumpos et al. have revealed the existence of ferroelectric properties in β-$MAPbI_3$ by observing hysteric behavior in the current-voltage curves [40]. Kutes et al. used PFM to accomplish the first direct observation of ferroelectric domains in solution-processed β-$MAPbI_3$ perovskite thin films with a grain size of ~100 nm [41]. They also observed the reversible switching of ferroelectric domains through direct current poling, as shown in Figure 4a. In addition, Kim et al. demonstrated the ferroelectric polarization behavior in $MAPbI_3$ perovskite under both dark and light illumination using PFM [109]. $MAPbI_3$ exhibited spontaneous polarization in the absence of an electric field

Accepted manuscript

ACCEPTED MANUSCRIPT

without a significant change in polarization based on crystal size, while the larger crystals exhibited longer retention behavior than smaller crystals. Rohm et al. used PFM imaging to elucidate the ferroelectric properties of $MAPbI_3(Cl)$ thin films by inspecting both vertical and horizontal images and observed that spontaneous polarization resulted in different orientations in the ferroelectric domains within a crystal [110]. Further, Rakita et al. demonstrated ferroelectricity in the tetragonal phase of $MAPbI_3$ by observing the inversion of polarization under an external applied field along with lack of inversion symmetry and the existence of spontaneous polarization [81]. Many research groups have used theoretical and experimental investigations to confirm ferroelectricity in OMHPs [111-114].

In addition to the commonly used Pb- and Sn-based OMHPs, (3-pyrrolinium)$CdCl_3$ and (benzylammonium)$_2PbCl_4$ exhibits ferroelectricity with spontaneous polarization at temperatures above room ambient [95,96]. Recently, in a breakthrough for OMHP ferroelectric materials, $Me_3NCH_2ClMnCl_3$ (TMCM-$MnCl_3$) synthesized using low-temperature solution process, exhibited an outstanding piezoelectric response (d_{33} = 185 pC/N) with a high Curie temperature of 406 K, which is comparable to inorganic piezoelectric $BaTiO_3$ (190 pC/N) [97]. As shown in Figures 4b and 4c, the ferroelectric domains of TMCM-$MnCl_3$ are clearly observed in the PFM phase and amplitude images. Many more studies are needed, however, to clearly understand the orientational dynamics of MA^+ cations, the dynamics of domains and domain walls, and the relationships between the polarization and rotational dynamics of MA^+ cations. However, the outstanding ferroelectric and optical properties of OMHPs offers promise for the further development of flexible optoelectronic and piezoelectric devices.

2.4. Piezoelectric properties

Accepted manuscript

ACCEPTED MANUSCRIPT

The piezoelectric effect has been referred to as a coupling between mechanical and electrical fields. Piezoelectricity is the ability of certain materials to generate electric potential under an applied mechanical stress and vice versa. The crystallographic requirement for the existence of piezoelectricity in a material is the lack of centrosymmetry. The OMHPs are a new class of perovskite family comprised of both organic and inorganic cations, which exhibits notable ferroelectric and piezoelectric properties that are relatively comparable to inorganic perovskite materials. The piezoelectricity of any piezoelectric material can be measured by its piezoelectric coefficient, which is proportional to the dielectric constant and polarization (i.e., $d_{33}\,\alpha\ \varepsilon_r P_r$) [115]. Coll et al. were the first to use PFM to experimentally explore the piezoelectric coefficient of polycrystalline OMHP films [42]. They observed an enormous increase in the piezoelectric coefficient (~ 25 pm/V) under illumination than the value measured under darkness (5-6 pm/V) as shown in Figure 5a, which attributed to the formation of large photo-induced dipole moments via molecular orientations of MA^+ cations. However, an inaccurate estimation of the tip contact area and other artifacts coming from surface topography and crystal orientation could limit local PFM study of the piezoelectric properties of polycrystalline films [116-119]. For direct evidence of the piezoelectric response, Dong et al. directly observed the piezoelectric effect in a single crystal of $MAPbI_3$ [120] and the measured effective piezoelectric coefficient (d_{33}) of 2.7 pm/V along the (001) direction, as shown in Figure 5b. In addition, Song et al. used PFM to investigate the effect of the interfacial screening layer on the piezoelectric response of polycrystalline $MAPbI_3$ films [121]. In that study, $MAPbI_3$ films revealed a higher piezoelectric coefficient (d_{33}) of ~ 4 pm/V when prepared on epitaxial PZT, whereas d_{33} values of $MAPbI_3$ films prepared on Au, indium tin oxide (ITO), and on $SrTiO_3$ surfaces were comparatively low as shown in Figure

Accepted manuscript

ACCEPTED MANUSCRIPT

5c, which was attributed to large-scale interfacial polarization that promotes polar alignment in polycrystalline $MAPbI_3$ films.

Liu et al. theoretically demonstrated that the calculated piezoelectric coefficient of $MAPbI_3$ in the polar configuration was higher than that in a non-polar configuration [43]. They deduced that the enhanced piezoelectric response under illumination was likely due to the light-induced molecular movement from a non-polar to a polar configuration in the presence of an electric field, as shown in Figure 5d. That result suggests that light illumination could weaken the hydrogen bond between the MA^+ cation and the Pb-I scaffold, which would allow the formation of a polar structure with aligned MA^+ cations in an electric field. Ding et al. used piezoresponse force spectroscopy (PFS) in an experimental investigation of the piezoelectric properties of $FAPbBr_3$ nanoparticles (NPs) [101]. In that study, $FAPbBr_3$ NPs exhibited the effective piezoelectric coefficient of ~ 25 pm/V, which was 5-fold higher than that of $MAPbI_3$ films. In addition, the piezoelectric coefficient of $MAPb_{1-x}Fe_xI_3$ films was investigated in our previous work by partially replacing Pb^{2+} with Fe^{2+}, which returned values of ~ 17.0 ± 6.0 pm/V that were more than 3-fold higher than that for $MAPbI_3$ films [44]. Furthermore, Huang et al. compared non-toxic, non-centrosymmetric 2D MA_2CuCl_4 perovskite with vertically aligned octahedron of $[CuX_6]^{4-}$ along the direction of the aligned organic cations. The MA_2CuCl_4 perovskite revealed a high piezoelectric coefficient of 49.51 pC/N in the (111) direction [122]. Recently, You et al. demonstrated toxic-free, single-phase TMCM-$MnCl_3$ with excellent ferroelectric and piezoelectric properties [97]. As shown in Figures 5e and 5f, TMCM-$MnCl_3$ revealed a larger piezoelectric coefficient (d_{33}) of 185 pm/V in the (102) direction of the crystal that was relatively comparable to few piezoelectric or ferroelectric materials. TMCM-$MnCl_3$ exhibited a phase-transition temperature (T_c) of 406 K that was comparatively higher than that of BTO [123].

Accepted manuscript

ACCEPTED MANUSCRIPT

Based on these observations, attractive piezoelectric properties and advantageous characteristics of OMHPs such as low temperature and cost-effective, simple-solution route techniques offer wide latitude for the design of implantable piezoelectric energy harvesters. However, numerous studies are required to realize the excellent piezoelectric properties of OMHPs via functional modification or newly designing, which could be a focal point for potential applications towards the mechanical harvesting of energy.

3. Synthesis of organic-inorganic metal halide perovskites

OMHPs have been widely used as the active material in energy-harvesting (i.e. photovoltaic and piezoelectric) and light-emitting devices because of their wide range of chemical tunability and relevant physical properties. Similar to the optoelectronic applications, the initial studies of OMHP-based PEGs were focused on polycrystalline thin films and low-dimensional nanocrystals, in which the control of OMHP crystallization is required to achieve the enhanced physical properties that are associated with their attributes such as chemical composition, morphology, grain size, crystallinity, and surface coverage [39,101]. Furthermore, the adoption of OMHPs into PEGs can be achieved by conventional solution processing or vacuum deposition to form polycrystalline thin films or by a wet-chemical method to synthesize a blend of polymeric materials and low-dimensional nanocrystals. Therefore, we approached our review of the synthesis of OMHPs by separately considering the work being pursued in (1) polycrystalline thin films and in (2) low-dimensional nanocrystals.

3.1. Polycrystalline thin films

Due to the low formation energy required to form a hybrid perovskite crystalline structure, OMHP polycrystalline films are generally prepared via low-temperature solution processes: 1)

Accepted manuscript

ACCEPTED MANUSCRIPT

one-step solution processing, 2) two-step sequential deposition, 3) vapor deposition, and 4) vapor-solution hybrid processing (Figure 6) [124-129]. The simplest method for the production of OMHP thin films utilizes OMHP crystallization from a precursor solution by spin-coating, dip-coating, spray-coating, or doctor-blading with subsequent thermal annealing to remove the residual solvent. A common precursor solution consists of CH_3NH_3X (methylammonium halide; MAX) and PbX_2 (X=Cl, Br, I) dissolved in a common polar solvent such as N,N-dimethylformamide (DMF), γ-butyrolactone (GBL), dimethyl sulfoxide (DMSO), or acetonitrile (Figure 6a) [124-126]. A two-step process of sequential solution processing was proposed for better control of the crystalline formation (i.e., to avoid wide morphological variations), in which the individual precursor is sequentially spin-coated onto the substrate (Figure 6b) [127]. Here, the second precursor can be applied not only by spin-coating but also by dip-coating [128]. For example, Burschka et al. converted $MAPbI_3$ by dipping PbI_2-coated TiO_2 mesoporous substrate into a MAI solution (Figure 6c) [29], which allowed highly loaded and densely packed OMHP film.

The development of a number of approaches to tune the composition, morphology, and crystallinity of OMHPs has led to significant progress in the synthetic route via control of the precursor solution (i.e., concentration and stoichiometry), solvent types, surface interactions, spin-coating conditions, and annealing conditions (i.e., temperature and duration) [29,129,130]. In particular, transition metal doping into OMHPs enhances their piezoelectric properties by increasing the dielectric constant of the host $MAPbI_3$ polycrystalline thin films, in which 7 at.% Fe incorporation was achieved via introduction into the precursor solution [44]. The $MAPbI_3$ grain size can be controlled by varying the concentration of the precursor solution (Figure 6d) [127]. To facilitate a uniform OMHP film with a densely packed, large-sized grain, a fast-

Accepted manuscript

ACCEPTED MANUSCRIPT

deposition crystallization process was developed by Xiao et al. (Figure 6e) [131]. Here, the immediate exposure of the spin-coated OMHP film to a poor solvent such as chlorobenzene facilitates a fast crystallization of the perovskite phase that arises from the rapid reduction of solubility. Moreover, fast-deposition crystallization approaches result in high crystallinity at room temperature, which allows low-temperature post-processing without further heat treatment. Additional synthetic routes to control film morphology include the addition of organic surfactants such as NH_4Cl and phosphatidylcholine [132]. The presence of surfactants in the precursor solution can lead to the formation of smooth films with a few layers of perovskites, where the sizes of the crystal domains are larger than the film thickness [132]. Based on the above-mentioned synthetic approaches, blade-coating and spray-deposition methods also extend the feasibility of using roll-to-roll coating to produce low-cost, mass-produced OMHP films with large-area coverage [132, 133].

While precise control of the morphology and chemical homogeneity of OMHP polycrystalline thin films is required to enhance performance, it is a challenge to prepare a reproducible and good-quality thin film by solution processing because accurate control of the deposition conditions is required. A dual-source vacuum deposition process of MAI and $PbCl_2$ was developed by Liu et al. (Figure 6f) [134] to achieve a uniform thin film with full surface coverage and a homogenous composition. Dual-source vacuum deposition allows control of the deposition rate for each of the precursors in order to precisely adjust the film thickness and final chemical composition. A two-step chemical vapor deposition process has also been used to fabricate $FAPbI_3$ film with a large-grain size [135,136]. Here, the precursors first were evaporated at high temperature under an inert gas flow, and then deposited to form a thin film (Figure 6g). These two main strategies (i.e., vacuum deposition and solution processing) have

Accepted manuscript

ACCEPTED MANUSCRIPT

been combined into a two-step hybrid approach for the formation of OMHP polycrystalline thin films [137].

3.2. Low-dimensional nanocrystals

In general, PEG responses to different types of physical strain (bending, extension, compression) require structural stability and flexibility under significant bending or twisting of OMHPs. OMHP nanocrystals can be incorporated into soft polymeric materials to improve mechanical durability under mechanical deformation, which makes them attractive candidates for flexible PEGs. In order to achieve optimal power output, the effective control of the composition and dimension of OMHP nanocrystals, as well as their uniform dispersion in the polymer nanocomposite, is a prerequisite for the technological utilization of OMHP nanocrystals.

Zeng et al. reported a facile method to prepare OMHP nanocrystals by ligand-assisted reprecipitation (LARP), in which a precursor solution of MAX and PbX_2 (X=Cl, Br, and I) in a good solvent (e.g., DMF, DMSO, etc.) is precipitated in a poor solvent (typically, toluene and hexane) under stirring, producing colloidal OMHP nanocrystals (Figure 7a) [138-142]. In particular, the formation of nanocrystals is attributed to the introduction of an organic surfactant such as long alkyl chains (commonly *n*-octylamine and oleic acid) into the precursor solution (Figure 7b). The LARP method was further extended to synthesize $FAPbBr_3$ [139], which was combined with a polymeric material to prepare a flexible PEG [101]. The size of OMHP nanocrystals is controlled by tuning synthesis conditions such as temperature [140], type of surfactants [141], and the ratio of the precursor solution in a poor solvent [142]. Furthermore, metal doping into OMHP nanocrystals can also be used to precisely tune their electrical,

Accepted manuscript

ACCEPTED MANUSCRIPT

optoelectronic, and piezoelectric properties. Arunkumar et al. reported that $MAPbBr_3$ nanocrystals could be doped with Mn up to 90% by substituting Pb with Mn while maintaining the identical crystal structure [143].

Li et al. [144] and Sun et al. [145] extended the LARP process to the synthesis of all-inorganic cesium lead halide ($CsPbX_3$, X = Cl, Br, I) perovskite nanocrystals, which are usually synthesized using a hot injection method [146]. Emulsion synthesis is an alternative method for the preparation of low-dimensional OMHP nanocrystals (Figure 7b) [147]. In this case, an emulsion of immiscible polar (e.g. DMF) and non-polar solvents (e.g. *n*-hexane) is prepared by using *n*-octylamine as a surfactant. Next, the addition of a de-emulsifier (acetone, tert-butanol, etc.) initiates a crystallization process that results in OMHP nanocrystals, the nanocrystal dimensions of which are controlled by adjusting the ratio of emulsifier and de-emulsifier. Facile synthesis of OMHP nanowires was reported by ultrasonication of the precursors (MAX, FAX, and PbX_2, X = Cl, Br, I in a non-solvent) in the presence of surfactants [148-150].

The aforementioned methods produce high-quality nanocrystals, but the production yield is too low to meet the requirements for practical application (0.1 ~ 0.15 g/cm^2 for 30 wt.% PEG with a thickness of 200 μm). For a large-scale synthesis of OMHP nanocrystals, a combination of solid-state ball milling, chemical exfoliation, and ultrasonication has been reported (Figure 7c). The Papavassiliou group was one of the first to report nanocrystal synthesis *via* the grinding of bulk perovskite materials [151]. Solid-state reactions produce a gram scale of OMHP micro and nanocrystals *via* the ball-milling technique [152,153]. Further reduction of OMHP crystal size can be facilitated *via* the ligand-assisted exfoliation of perovskite bulk powders [154] since the OMHPs easily undergo exfoliation, which results in layered OMHP nanocrystals with different thicknesses and the relevant physical properties [155]. More recently, a scalable

Accepted manuscript

ACCEPTED MANUSCRIPT

synthesis process has produced OMHP nanocrystals of 10 g or larger depending on the batch size of the ball-milling instrument (Figure 7d) [156].

For a flexible PEG based on polymer nanocomposites, the incorporation of OMHP nanocrystals into polymeric materials can be achieved by 1) a simple blending, 2) nanocrystal growth within a polymer matrix, and 3) in-situ polymerization in the presence of nanocrystals [157-161]. For example, high-performance (8.5 V and 3.8 μA cm^{-2}), flexible PEGs have been synthesized using a blend of polydimethylsiloxane (PDMS) and formamidinium lead halide perovskite ($FAPbBr_3$) nanocrystals (~ 50 nm, 35 wt.%) [101]. Recently, MA_2CuCl_4 perovskite nanocrystals were embedded into PVDF for use as a PEG. In particular, MA_2CuCl_4 showed output power that was higher than that of $MAPbBr_3$, possibly arising from the large Cu off-centering displacement [122]. It should be noted that a MA_2CuCl_4/PVDF nanocomposite was prepared via the in-situ synthesis of MA_2CuCl_4 nanocrystals in PVDF. Directly grown perovskite nanocrystals in a polymer matrix enable a higher number density of OMHP nanocrystals in nanocomopsites without sacrificing the benefits of nanocrystal morphology [159].

4. Piezoelectric generators based on organic-inorganic metal halide perovskites

Piezoelectric materials have attracted much attention as active materials for use in a range of devices such as transducers, actuators, self-powered sensors, piezoelectronics, and energy harvesting devices. Among these devices, PEGs are extensively utilized for scavenging energy from ambient mechanical energy sources and converting it to usable electrical energy [162]. In recent years, numerous PEGs have been constructed using various types of piezoelectric materials including ZnO nanostructures, GaN nanowires, PZT, $BaTiO_3$, and piezoelectric polymers. Among these materials, perovskite ceramics are considered the most favorable

Accepted manuscript

ACCEPTED MANUSCRIPT

candidates for the construction of high-performance PEGs due to their excellent piezoelectric properties. However, these inorganic piezoelectric materials require complicated synthesis processes such as high-temperature calcination and sintering. Unlike the inorganic perovskite materials, OMHPs have utility with a variety of metal substrates and numerous flexible polymer substrates without the need of a transfer process due to cost-effectiveness and low temperature-based, simple-solution processing. Many researchers have investigated the piezoelectric and ferroelectric properties of OMHPs, revealing that these OMHPs are the potential candidates for piezoelectric energy harvesting applications.

4. 1. OMHP-based piezoelectric generators

4. 1-1. $MAPbI_3$-based piezoelectric generators

OMHPs are beginning to garner a notable amount of attention in the field of energy harvesting *via* piezoelectric nanogenerators. In 2015, Kim et al. first experimentally observed the piezoelectric output performance of $MAPbI_3$ perovskite thin films by fabricating conventional PEG using flexible polymer substrates [39]. Fabrication of $MAPbI_3$-based PEG involved the integration of $MAPbI_3$ deposited Au/Ti-Polyethylene terephthalate (PET) substrate with PDMS-coated ITO-PET substrate. To explore the piezoelectric output performance of PEGs, a fabricated PEG was measured by applying mechanical pressure of 0.5 MPa normal to its surface with an active area of 1×1 cm^2. The device poled at 80 kV/cm exhibited the high peak voltage of 2.7 V with a current density of 140 nA/cm^2. The working mechanism of a $MAPbI_3$ perovskite-based PEG is shown in Figure 8a [39]. When a PEG is subjected to mechanical pressure, the mechanical stress can induce piezoelectric charges in the active layer, which results in a potential difference between the top and bottom electrodes. This induced piezopotential forces electrons to

Accepted manuscript

ACCEPTED MANUSCRIPT

flow from the bottom to the top electrode via an external load until accumulated charges balance the piezoelectric potential and create a positive voltage/current signal. Once the mechanical stress is released, the disappearance of the piezopotential in $MAPbI_3$ leads to a back-flow of electrons through the external circuit, which creates a negative voltage, or current signal. In the working mechanism of this device, an insulating PDMS layer provides a large potential barrier, which prevents electron transport through the active $MAPbI_3$ layer between two electrodes. For a non-poled PEG, the net-generated piezopotential will be relatively small due to randomly oriented dipoles in the piezoelectric layer. However, the electrical poling process can align the dipole orientation thus creating high piezoelectric potential in the $MAPbI_3$ layer under an applied pressure, which leads to an enhancement of output performance.

4.1-2. Fe^{2+}-incorporated $MAPbI_3$ flexible piezoelectric generators

The modest output performance of $MAPbI_3$-based PEG has been limited to the application of PEG. The development of high-performance, flexible nanogenerators for practical applications have been challenging. Recently, Liu et al. theoretically investigated and demonstrated controllable tuning of the structural, optical, electrical, and magnetic properties of OMHPs by substituting ABX_3 atomic constituents with various functional materials [43]. In particular, by comparing OMHPs with various atomic substitutions in the ABX_3 structure, they clearly demonstrated that displacement of the B-site cation contributes to virtually all the piezoelectric response, and the competition between B-X metal-halide bonds and organic cation-halide (A-X) hydrogen bonds in OMHPs controls the piezoelectric properties. These results were a challenge to elucidate the high piezoelectric properties of OMHPs *via* functional substitution/replacement. Our group seized on this clear demonstration, and systematically observed the dielectric and piezoelectric properties of $MAPbI_3$ perovskite by partially incorporating Fe^{2+} ions into the

Accepted manuscript

ACCEPTED MANUSCRIPT

$MAPbI_3$ structure, and enhanced the piezoelectric output performance with various volume fractions of Fe^{2+} [44]. In our study, we demonstrated that the partial replacement of Pb^{2+} with Fe^{2+} improved the morphological and crystalline properties as well as the dielectric, ferroelectric, and piezoelectric properties were linearly increased with increases in the Fe^{2+} concentration. These results suggest that the high dielectric and piezoelectric properties of $MAPb_{1-x}Fe_xI_3$ films strongly influence the generation of piezoelectric potentials by enhancing the piezoelectric output performance. A clear explanation is provided in the dielectric and piezoelectric properties section. To realize the piezoelectric output performance of Fe^{2+}-incorporated $MAPbI_3$ films, we fabricated flexible $MAPb_{1-x}Fe_xI_3$ ($0 \leq x \leq 0.07$)-based PEGs by incorporating various concentrations of Fe^{2+}. The device fabrication and power generation mechanism of PEG is similar to that of $MAPbI_3$-based PEG. Figures 8b and 8c show the schematic diagram of a $MAPb_{1-x}Fe_xI_3$-based PEG structure and the captured images of fabricated PEG, respectively, which also reveals its flexibility by bending with fingers. The measured piezoelectric output performance of non-poled $MAPb_{1-x}Fe_xI_3$ PEGs ($0 \leq x \leq 0.07$) was linearly increased with increases in Fe^{2+} concentration and attained maximum performance with incorporation concentration of $x = 0.07$, as shown in Figure 8d. The values for average peak output voltage and current density of a non-poled $MAPb_{1-x}Fe_xI_3$ ($x = 0.07$)-based PEG were ~ 4.52 V and 0.50 $\mu A/cm^2$, respectively, which was 6.2 times higher than that of a pristine non-poled $MAPbI_3$ PEG. Furthermore, the output performance of a $MAPb_{1-x}Fe_xI_3$ ($x = 0.07$)-based PEG was enhanced by poling the device at an applied field of 30 kV/cm. The poled PEG revealed high output voltage and current density of ~ 7.29 V and 0.88 $\mu A/cm^2$, respectively. This level of performance was sufficient to instantly power a commercial red LED without the need of a storage device, as shown in Figure 8e. This approach provides a framework for designing functional OMHP

Accepted manuscript

ACCEPTED MANUSCRIPT

piezoelectric materials with robust optical tunability and could be potential candidates for the development of a wide range of portable, self-powered, and wearable electronic devices.

4. 1-3. Pressure and light sensitive bimodal sensors via Piezo-photoelectric $MAPbI_3$ perovskite thin films

Moreover, apart from the excellent piezoelectric properties explained in former sections, OMHPs have drawn a considerable amount of attention in the fields of optical sensors and light-driven electromechanical transistors owing to their excellent optical absorption properties. Coll et al. observed the polarization switching and dependence of piezoelectricity on photogenerated carriers upon light irradiation in lead based OMHPs. Their results emphasized the increase in piezoelectric polarization under illumination in $MAPbI_3$ perovskite [42]. Eom et al. reported self-powered pressure and light-sensitive bimodal sensor based on stable $MAPbI_3$ perovskite thin films fabricated *via* a chemical vapor deposition method (CVD) [163]. They found that CVD-$MAPbI_3$ samples revealed excellent stability while samples prepared *via* solution processing using polar solvents such as DMF and DMSO retained a low stability due to the existence of intermediate complexes *via* interactions with humidity via the formation of hydrogen bonding due to an intrinsic hydrophilic nature. Stable $MAPbI_3$ thin films were synthesized on PET or glass substrates using two zones chemical vapor deposition equipment by controlling the flow rates of PbI_2 and MAI, as clearly sketched in Figure 8f. For the fabrication of pressure and light-sensitive bimodal sensor, transparent and flexible Al (3%)-doped ZnO (AZO)/Au/AZO thin films were sputtered onto PET or glass substrates using radio-frequency (*rf*) facing target sputtering and direct-current (*dc*) sputtering as a bottom electrode followed by the deposition of $MAPbI_3$ perovskite film using the CVD method. A 50 nm-thick SiO_2 layer sputtered onto $MAPbI_3$/AZO/Au/AZO/PET films was followed by the deposition AZO/Au/AZO as a top

Accepted manuscript

ACCEPTED MANUSCRIPT

electrode, as shown in Figure 8g. Here, the SiO_2 layer acts as an insulator to prevent the ion migration of I^- and MA^+ ions between two electrodes under applied mechanical pressure due to low activation energy. Finally, polytetra fluoroethylene (PTFE) thin film was sputtered onto the device in order to protect the device from humidity and to eliminate the triboelectric effect that rises from electrodes. In order to measure the piezoelectric output performance, the device was poled at 60 kV/cm with an active layer area of 0.4 × 0.4 cm^2. The measurement was performed using a 10 MΩ load resistance under applied pressures ranging from 5 to 70 kPa with an applied frequency of 0.4 Hz. The results show that the output voltage and current were linearly increased with increases in applied pressure and were saturated above an applied pressure of 40 kPa. As shown in Figure 8h, the sensitivity of the pressure sensor was ~ 8.43 mV/kPa. Furthermore, to investigate the pressure and light-sensitive bimodal characteristics of $MAPbI_3$ piezoelectric films, the device was exposed to varied intensities of light at an applied pressure of 30 kPa. The output performance of the device showed a strong dependence on the intensity of the illumination. These types of bimodal sensing devices could be the components for new self-powered device applications such as portable electronics and wireless sensors.

4. 1-4. Single structured TPS-fusion energy harvester via $MAPbI_3$ perovskite thin films

The emergence of OMHPs has drawn much attention for various applications owing to promising characteristics such as an ambipolar nature, a ferroelectric nature, and ultra-high Seebeck coefficients. These exclusive properties render OMHPs useful as fusion energy conversion materials for the harvesting of ambient forms of energy such as thermal, mechanical and solar for the development of integrated energy harvesting systems. However, the integration of two or more harvesters such as a solar cell with a PEG or a TEG as a single energy harvester that can convert more than one energy source into electricity could increase both the complexity

Accepted manuscript

ACCEPTED MANUSCRIPT

and the volume. This key motivation encouraged our introduction of a flexible single-structured TPS (thermoelectric, piezoelectric, and solar)-fusion energy device comprised of interdigitated electrodes (IDEs) and $MAPbI_3$ that could be useful in harvesting thermoelectric, piezoelectric, and solar energy [45]. Moreover, Park et al. reported that an IDE-based PZT nanogenerator generated an output performance that was higher than metal-piezoelectric (insulator), (MIM)-based devices by introducing a flexible, highly efficient large-area, PZT thin-film-based nanogenerator [164]. They confirmed that the introduction of IDEs as electrodes on a PZT thin film provides a tool for utilizing the piezoelectric d_{33} mode, which is two times higher than the d_{31} mode and led to an enhancement in the output performance of nanogenerator. Thus, IDE-based TPS-fusion energy devices can be utilized to generate higher output performance using $MAPbI_3$ as piezoelectric material [45]. TPS-fusion device was fabricated according to the schematic procedure shown in Figure 9a. $MAPbI_3$ perovskite thin film was spin coated onto a flexible PET substrate followed by deposition of Cu_2O, ZnO and ITO thin films via sputtering using metal masks. Finally, the TPS device was encapsulated using a spin-coated PDMS layer to prevent the perovskite dye from ambient conditions and to increase the mechanical endurance of the device. A captured digital image and an optical image with measured dimensions of the TPS-device are shown in Figures 9b and 6c, respectively. Figure 9d depicts the schematic cross-section of one pair of IDE electrodes on the $MAPbI_3$ film of the TPS device with an inter-electrode gap of 500 μm and the measured SEM cross-sectional images of a fabricated device with each IDE electrode. The piezoelectric output performance of the TPS device was measured under an applied pressure of 0.2 MPa with an input impedance of 10 MΩ at a frequency of 5 Hz after poling the device in a 12 kV/cm field. The piezoelectric output voltage and current values of poled device were ~ 1.47 V and ~ 0.56 μA, respectively, as shown in Figure 9e. Further, the

Accepted manuscript

ACCEPTED MANUSCRIPT

same PEG was tested by finger tapping and exhibited relatively high output voltage and current of ~ 0.47 V and 0.14 μA, respectively.

The TPS-fusion energy device working mechanism of a PEG is depicted in Figure 9f [45]. Initially, the electric dipole charges were randomly distributed in polycrystalline $MAPbI_3$ perovskite films. The semiconductor ZnO and Cu_2O layers deposited onto $MAPbI_3$ can align the dipoles that exist in the $MAPbI_3$ layer, but the resultant alignment might not be uniform. However, the poling process can modify the orientation of the dipoles to the applied field direction in the active layer, and as a consequence the polarization direction of the diploes becomes parallel to the surface of the piezoelectric material and results in a higher level of device performance. When mechanical stress was applied to the surface of the generator, the applied pressure was uniformly transferred to the perovskite film through the PDMS layer and resulted in charge generation due to the combined tensile and bending stress in a manner similar to reports in the literature based on PZT nanofiber piezoelectric generators [165]. These generated charges create a potential difference between the neighboring electrodes and allows electrons to flow through the external circuit and generate positive voltage or current signals. When mechanical stress was released from the device the piezopotential at each pair of electrodes disappeared and electrons flowed back to the original state, which generated negative voltage, or current, signals. Furthermore, this single-structured IDE based TPS-device can also be utilized to harvest thermal, mechanical, and solar energy from ambient conditions. These results suggest that the further development of this flexible, IDE-based simple fusion energy conversion device with suitable light active ambipolar materials could introduce an innovative framework for fusion energy harvesting technology, which could thereby be applied to self-powered and wearable electronic systems.

Accepted manuscript

ACCEPTED MANUSCRIPT

4.2 OMHP-polymer composite-based piezoelectric generators

Generally, ceramic piezoelectric material-based nanogenerators are emerging as promising tools for scavenging mechanical energy because of their outstanding piezoelectric properties. However, practical implantation and versatile utilization in various flexible, wearable, and biocompatible electronic devices is severely restricted and limited due to their brittle and rigid nature under applied large strain and harsh environment. Thus, extending the flexibility of these nanogenerators would render them useful for a wide range of applications in the field of energy harvesting technology. By comparison, polymer-based piezoelectric materials, such as cellulose, poly (L-lactic acid) (PLLA), PVDF, and similar copolymers, are beneficial alternatives for piezoelectric applications because of advantageous properties such as high mechanical strength, desirable flexibility, cost effectiveness, good chemical stability, and ease of processing to desired shapes [166-169]. Hence, the development of polymer composite-based nanogenerators is pivotal to solving the inflexibility problem. Similar to ceramic materials, OMHPs are brittle and inflexible. Consequently, using flexible polymers and perovskite materials to fabricate hybrid composite-based PEGs is expected to significantly enhance their flexibility. Moreover, the flexibility of piezoelectric energy harvesters shows remarkable endurance under applied strain, which allows enormous output performance under large strain caused by off-resonance vibration and uniform deformation. Several researchers have focused on developing hybrid composite PEGs that are based on flexible polymers and inorganic piezoelectric active materials to obtain high performance with excellent mechanical robustness [170-174]. Our group, and others, has developed flexible and highly stable polymer composite-based PEGs via the introduction of OMHPs into polymer matrices such as PDMS and PVDF, which is described in the next section [100,175-177].

Accepted manuscript

ACCEPTED MANUSCRIPT

4. 2-1. OMHP-PDMS polymer composite-based piezoelectric generators

High-performance, flexible hybrid composite PEGs based on $FAPbBr_3$ and PDMS polymer composite films were first realized by Ding et al. [101]. Those composite films were comprised of a flexible PDMS polymer matrix and uniformly distributed $FAPbBr_3$ nanoparticles. Well-developed ferroelectric properties were accomplished by switching the polarization. Various flexible piezoelectric nanocomposite generators were fabricated by sandwiching the composite film between an ITO-coated PET substrate and aluminum foil with various weight ratios of $FAPbBr_3$ nanoparticles in the polymer matrix. Schematic diagrams of a composite-based device and an SEM cross-sectional image of the fabricated device with an active piezoelectric layer thickness of 150 µm appear in Figures 10a and 10b, respectively. Output performance was monitored by applying 0.5 MPa of vertical compression at a frequency of 6 Hz to devices poled at 50 kV/cm. The device with 35 wt. % of $FAPbBr_3$ particles revealed a maximum output voltage of 8.5 V and a current density of 3.8 $\mu A/cm^2$, respectively, as depicted in Figure 10c. The generated high output was stored in a capacitor and applied to brighten a commercial red LED. In addition, Dhar et al. reported another polymer composite nanogenerator based on $MAPbI_3$ and PDMS polymer by observing significant lattice-defect-induced piezoelectric responses in $MAPbI_3$ perovskite particles [99]. Figure 10d shows the SEM surface image of the $MAPbI_3$ perovskite particles prepared using a ball mill grinding technique. These particles were utilized to fabricate composite film-based nanogenerators via uniform dispersion in a PDMS solution that maintained a composite film thickness of 0.1 cm. Composite films were integrated between two aluminum foils for use as electrodes, and the device was sealed with a thin PDMS layer after these electrodes were wired. Figures 10e and 10f show a schematic diagram of the nanogenerator and a snapshot of the fabricated device, respectively, which depicts an admirable level of

Accepted manuscript

ACCEPTED MANUSCRIPT

flexibility during finger twisting. The piezoelectric output performance of various composite films was measured via finger manipulation, which showed that devices prepared using $MAPbI_3$ perovskite (FPENG30) grinded for 30 min exhibited a higher voltage of 108 V with maximum power density of 0.3 mW/cm^3. These results emphasized how smaller particle sizes produced a higher lattice strain that governed the Pb^{2+} vacancy defects. The higher level of defect-dependent ionic polarization in 30 M-$MAPbI_3$ perovskite films was confirmed via positron annihilation spectroscopy (PAS). Along with the defect-dependent polarization studies, the output trend can be explained by using the dielectric properties of composite films, which is clearly explained in the dielectric sections. Based on the dielectric and P-E measurements, composite films comprised of 30 M-$MAPbI_3$ revealed high dielectric constant and polarization, which translated to higher output performance. Furthermore, output energy generated with FPENG30 instantly lit 30 commercially available blue LEDs connected in series via a full-wave bridge rectifier under gentle finger manipulation. These results expand the possibilities for a wider range of implantable touch-sensing applications for OMHPs.

4. 2-2. OMHP-PVDF polymer composite-based piezoelectric generators

Due to the highly viscous nature of PDMS, however, prepared perovskite particles may not uniformly distribute in a PDMS matrix, which could result in modest interactions between PDMS and $MAPbI_3$ perovskite particles that would reduce the output performance of PEGs. Lower output device performance causes extensive anxiety in practical applications. PVDF polymers are commonly used as piezoelectric polymer materials because of their remarkable flexibility and excellent piezoelectric properties. Ding et al. demonstrated a high-performance, flexible PEG based on $FAPbBr_3$ nanoparticles and PVDF polymer composite films [175]. $FAPbBr_3$-PVDF composite film-based devices were fabricated by integrating annealed

ACCEPTED MANUSCRIPT

composite films between two Au/Cr-coated PET substrates with a thin layer of spin-coated PDMS, as shown in Figure 11a. An SEM cross-sectional image of the fabricated device with a composite layer thickness of 120 μm appears in Figure 11b, and Figure 11c shows an enlarged surface cross-sectional view that depicts the random distribution of $FAPbBr_3$ particles in the PVDF matrix. Before measuring the piezoelectric output performance, the composite-based device was poled at 50 kV/cm. Values for the obtained output voltage and current density of the 12 wt % $FAPbBr_3$-PVDF composite generator were 30 V and 6.2 $\mu A/cm^2$, respectively, at an applied vertical pressure of 0.5 MPa with a frequency of 5 Hz. Generated output was used to charge a capacitor and was applied to light a red LED *via* a bridge rectifier. Sultana et al. demonstrated a piezoelectric energy harvester (PEH) that was based on $MAPbI_3$ and PVDF polymer composite films [176]. $MAPbI_3$ and PVDF composite films were prepared by homogeneously mixing synthesized $MAPbI_3$ particles in a PVDF solution. Results showed that the electro active β-phase of PVDF was enhanced by compositing PVDF with OMHPs due to enormous interactions between perovskite particles and PVDF stock. Figure 11d depicts a schematic diagram of the interactions between the $MAPbI_3$ and PVDF polymer. The electronegative iodine atoms of the perovskite framework electrostatically interacted with $-CH_2$ dipoles in the PVDF matrix, which facilitated the nucleation of electroactive phases. Electrostatic interactions tend to form a continuous dielectric layer at the polymer-perovskite interface, and this initiates a preferable nucleation of the electroactive phase by inducing the β-phase throughout a composite film. Piezoelectric composite generators based on $MAPbI_3$ and PVDF were fabricated according to the schematic diagram shown Figure 11e. The output voltage of the device was 1.5 V recorded by applying mechanical stress from a human finger without electrical poling prior to the measurement, as shown in Figure 11f. The same fabricated films were utilized

Accepted manuscript

ACCEPTED MANUSCRIPT

to fabricate a hybrid device, which amounted to a light active piezoelectric energy harvester that could be used as a flexible self-powered visible light detector/sensor. These results unambiguously show that OMHP composite-based generators are candidates for flexible light-sensing applications.

Sultana et al. synthesized a piezoelectric nanofiber mat via an electrospinning process that introduced $MAPbBr_3$ particles into a PVDF solution that was then used to fabricate a flexible PEG [177]. The SEM surface image in Figure 11g shows uniform and dense nanofibers that were prepared *via* electrospinning a $MAPbBr_3$-PVDF solution at 7 kV/cm. The fabricated composites generated an open circuit voltage of ~ 5 V from a vertical finger-touch motion on a device. The composite device could also be utilized as an acoustic nanogenerator (ANG) to detect noise. The instantly recorded output voltage was 5 V at an applied sound pressure level of 85 dB, as shown in Figure 11h. Along with the instantaneous output voltage, some applications demanded charging by a capacitor using a full-wave bridge rectifier when the ANG was subjected to acoustic vibrations. The stored energy was sufficient to drive a commercial LED strip and a wristwatch (Figure 11i). The resultant acoustic sensitivity of 13.8 V/Pa showed that the ANG was feasible for the monitoring of noise pollution. This approach introduces the development of noise detecting devices based on OMHPs generators for use as components in applications such as implantable sensing, biomedical devices, and portable electronics.

Based on the above discussions, all the fabricated OMHPs and polymer-based composite generators were comprised of active perovskite particles and polymer matrices. The distribution of piezoelectric particles may not be highly uniform in polymer frameworks due to the high viscosities of the polymer stock and the processing methods that are the main cause of moderate performances. Furthermore, Park et al. also reported a flexible nanocomposite generator (NCG)

Accepted manuscript

ACCEPTED MANUSCRIPT

based on PZT nanoparticles, PDMS, and carbon nanotubes [174]. These researchers observed that the output performance of the generator was enormously enhanced by adding CNTs as dispersing agents into the composite matrix of PZT-PDMS films because of the homogeneous dispersion of piezoelectric particles in a polymer. The CNTs act not only as dispersing agents but also as a conduction path throughout the composite matrix to enable the improvement of output performance of NCGs. Thus, the crucial aspect in governing the high output power of composite-based PEGs depends on the distribution and quantity of OMHP particles in a polymer matrix. Therefore, we recently took advantage of the most commonly used simple-solution processing of OMHP precursors to realize extremely uniform $MAPbI_3$-PVDF composite films and to develop high-performance, flexible, and stable $MAPbI_3$-PVDF composite-based piezoelectric energy harvesters [100]. Homogeneous $MAPbI_3$-PVDF composite films were prepared using a simple solution technique by homogeneously mixing of as-prepared $MAPbI_3$ precursor solution and a PVDF solution with various volume fractions of $MAPbI_3$ precursor. Prepared composite films revealed an excellent distribution of $MAPbI_3$ NPs in the PVDF by forming a uniform $MAPbI_3$-PVDF flexible matrix, as depicted in the SEM-EDS images in Figure 12a. Moreover, the electroactive β-phase of PVDF was improved by compositing with $MAPbI_3$ due to stronger electrostatic interactions, as explained in an earlier discussion. In addition to an increased β-phase, dielectric and ferroelectric properties were also significantly increased along with enhancement of the long-term stability of composite films, which is a key factor for commercial applications. For device fabrication, the composite films were integrated between ITO-coated PET and Au/Ti-PI substrates with a thin PDMS layer.

The power generation mechanism for OMHPs and polymer composite-based PEGs appears in Figure 12b [100]. This working mechanism is similar to all inorganic piezoelectric ceramic

Accepted manuscript

ACCEPTED MANUSCRIPT

materials and polymer composite-based nanogenerators. The initial stage shows no charge accumulation on the electrode surfaces of a PEG. When force is applied normally to a PEG, the generated piezoelectric potentials in crystalline PVDF enable the development of macro-dipoles in the filled $MAPbI_3$ particles, which results in the accumulation of charges with opposite polarity at the $MAPbI_3$-PVDF interfaces and surfaces. Further compression leads to greater change in piezopotential that causes electrons to flow from the bottom to the top electrode through an external circuit until the accumulated charges balance the piezopotential, which generates a positive voltage/current signal. During the release of applied pressure, relaxation of the $MAPbI_3$-PVDF matrix increases the charge density on both electrodes, which leads to a flow of charges from the top to the bottom electrode and generates a negative voltage/current signal. The piezoelectric output performance is measured by applying 0.5 MPa pressure normal to the PEG at a constant frequency of 5 Hz with an active area of 1×1 cm^2. PEGs poled at 80 kV/cm reveal better performance compared with non-poled devices. The PEG with 25 vol% of $MAPbI_3$-PVDF exhibit higher output voltage and current density of ~ 45.6 V and 4.7 $\mu A/cm^2$, respectively, with an active composite layer thickness of ~ 97.7 μm, as shown in Figures 12c and 12d, respectively. The generated power was sufficient to instantly light 10 green commercial LEDs without the need of a storage device, as shown in Figure 12e. Although the PEG showed a higher level of performance, in order to confirm the capability of PEG for the practical application of portable and wearable electronic devices, the output performance of the device was measured via finger tapping. The voltage and current values reached 18.5 V and 1.5 μA, respectively. This high output was used to instantly power 5 green LEDs via finger tapping of the PEG without the use of a storage device, as shown in Figure 12f. We unambiguously demonstrated that fabricated $MAPbI_3$-PVDF-based PEGs are viable candidates as energy sources

Accepted manuscript

ACCEPTED MANUSCRIPT

for the low-power consumption required by small-scale electronic devices. In addition, Huang et al. recently reported a PEG that was based on less-toxic MA_2CuCl_4/PVDF composite films via the in-situ fabrication of copper halide perovskite nanocrystals embedded in PVDF solution by mixing their precursor solutions [122]. The piezoelectric properties of composite films were investigated using PFM and DFT calculation, and the piezoelectric response of optimized MA_2CuCl_4/PVDF composite films was higher than that of pure PVDF films. The enhancement was attributed to a large amount of Cu off-centering displacement and to the strong interactions between MA_2CuCl_4 and PVDF, as clearly explained in former sections. In order to explore the potential of MA_2CuCl_4/PVDF composite films in piezoelectric devices, output power was measured by periodically applying pressure to the composite film-based PEG sandwiched between ITO and Al electrodes. Interestingly MA_2CuCl_4/PVDF composite films revealed higher output performance than either pure PVDF films or $MAPbBr_3$/PVDF films owing to the greater stress concentration around the perovskite particles in the composite films. This simple and cost-effective solution process is feasible for the fabrication of large-scale, high-performance OMHP composite-based PEGs with high flexibility, durability, and enormous stability which makes them well suited for a wide range of wearable and self-powered electronics.

Despite the relatively small piezoelectric properties of OMHPs, by comparison with conventional ceramic materials, OMHPs and their polymer composites have the remarkable and notable advantages of cost-effective production, ease of processing, light weight, and being mechanically flexible and compatible with large-scale roll-to-roll manufacturing. Such assets make them an extremely viable material choice and technologically interesting for use in large-scale flexible and wearable electronics that can be self-powered by simultaneous operations that involve the harvesting of solar, thermal, and mechanical energy.

Accepted manuscript

ACCEPTED MANUSCRIPT

5. Summary and perspectives

The development of sustainable energy sources to drive self-powered and portable devices is an ever-present challenge in energy research. Mechanical energy is one of the major sustainable energy sources that can convert ambient abundant energy into usable electricity via the piezoelectric effect. PEGs have received much interest in recent energy research due to admirable levels of electromechanical conversion that gives them viability for many integrated applications. In this review, the recent progress of flexible PEGs based on OMHPs is summarized in a systematic investigation of the crystal structure, dielectric, ferroelectric and piezoelectric properties of OMHPs. OMHPs possess a power conversion efficiency of more than 22% and represent a breakthrough in the field of photovoltaic applications. Besides the photovoltaic applications, OMHPs have the potential to replicate breakthrough performances in piezoelectric and ferroelectric applications owing to outstanding dielectric and piezoelectric properties that are relatively comparable to those of inorganic piezoelectric materials. Although most widely used piezoelectric materials are inorganic perovskites with strong spontaneous polarization and excellent electromechanical conversion, these materials have challenges for use in flexible/wearable devices and as bio-implanted sensors due to their complicated synthesis, high-temperature processing, and negligible degrees of mechanical flexibility. These problems can potentially be solved using OMHPs with advantageous characteristics such as facile low-temperature processing and by combining the characteristics of organic and inorganic solids at a molecular level due to their distinct structure. With advantageous solution-based processing at room temperature, OMHPs are suitable candidates for the fabrication of large-area flexible substrates in large-scale applications, which gives them compatibility with the integration of flexible generators with other electronic devices in self-powered flexible systems. Although

Accepted manuscript

ACCEPTED MANUSCRIPT

reports of PEGs based on OMHPs are limited to date, we anticipate significant advances and the production of highly efficient flexible nanogenerators in the near future as a great platform for sustainable energy harvesting.

The development of efficient flexible PEGs based on OMHPs and foreseeable implementation in various applications requires consideration of the following essential experimental features and additional research aspects. Greater effort must be invested in resolving these issues and constraints.

a) Improving the performance of PEGs for mechanical energy harvesting. Thoroughly investigating and understanding the ferroelectric and piezoelectric properties of OMHPs along with factors involving mechanical quality factor, electromechanical coupling, and energy conversion mechanisms will enable an enhancement of the output performance of nanogenerators.

b) Investigating the photoinduced ferroelectric and piezoelectric responses of OMHPs for the design of photoferroelectrics and photopiezoelectrics. The prior results have demonstrated that OMHPs are strongly influenced by illumination, which results in significant giant dielectric and piezoelectric responses likely due to the nonpolar to polar structural transition [42,94]. Few reports have focused on the use of these responses for piezoelectric energy harvesting applications, and more studies must be carried out to understand the photoinduced effect on piezoelectric energy harvesting.

c) Studying the structural tunability effect on ferroelectric and piezoelectric properties. Structurally modifying or tuning functional materials in OMHPs can significantly alter the structural, optical, dielectric and piezoelectric properties. For example, as theoretically

Accepted manuscript

ACCEPTED MANUSCRIPT

demonstrated by replacing MA^+ with a more polar molecular cation ($CF_3NH_3^+$), the polarization and piezoelectric responses are greatly increased, which makes OMHPs a potential candidate for piezoelectric energy applications [43]. Thus, the experimental realization of functionally modified OMHPs should pave the way for the design of high-energy conversion devices that are efficient.

d) Developing hybrid energy harvesters for multi-source energy harvesting. Ferroelectric materials are referred to as a subclass of pyroelectric and piezoelectric materials. It is suggested that OMHPs possess pyroelectricity. Rakita et al. observed the pyroelectricity in $MAPbI_3$ *via* a periodic temperature change method [81]. Further studies and experimental observations are required to understand the pyroelectricity of OMHPs, which could help in the design of a single hybrid energy generator to harvest multi-modes of energy.

e) Development of eco-friendly, flexible, high-performance PEGs. Despite the revolutionizing of photovoltaic solar energy conversion and rapid progress in numerous applications, OMHPs have seen limited commercialization due to instability and toxicity. Theoretical investigations have predicted that replacing Pb with Sn in OMHPs will result in improved piezoelectric properties for Sn-based perovskites that should render them relatively comparable to inorganic ceramics [43]. Until now, however, no experimental result has been published to establish the piezoelectric properties of Sn-based OMHPs. Limited studies have focused on Sn-based perovskites either for piezoelectric applications or for photovoltaic applications due to stability issues compared with Pb-based OMHPs. Thus, paying greater attention to replacing toxic elements in OMHPs with environmentally favorable materials should make them feasible for the development of eco-friendly PEGs for use in medical and biomechanical applications.

Accepted manuscript

ACCEPTED MANUSCRIPT

f) Enhancing the stability of OMHPs. One major concern, or challenge, that is associated with OMHPs is stability. Even though OMHPs have exhibited revolutionary performances in a number of applications, their lack of stability imposes challenges for commercialization. With continuous effort to increase the stability and significant advances, OMHP-based devices are expected to appear in our daily lives in the near future.

In conclusion, with increased amounts of research effort focused on improving stability and elucidating the ferroelectric and piezoelectric properties of OMHPs, one could reasonably anticipate significant advancements in the development of highly flexible and efficient OMHP-based devices, as well as wide-spread multifunctional applications.

Acknowledgements

This work was supported by a National Research Foundation of Korea (NRF) grant funded by the Korean government (MSIP) (No. NRF-2018R1A2A1A05018536) and by the Institute for Information & Communications Technology Promotion (IITP) grant funded by the Korean Government (Ministry of Science, ICT and Future Planning, MSIT, Grant No. 2017-0-00052), Omni-sensory smart physical sensor original technology for human body sensing and diagnosis.

References

[1] K. Dong, J. Deng, W. Ding, A.C. Wang, P. Wang, C. Cheng, Y.C. Wang, L. Jin, B. Gu, B. Sun, Z.L. Wang, Adv. Energy Mater. (2018) 1801114.

[2] A. Datta, Y.S. Choi, E. Chalmers, C. Ou, S. Kar-Narayan, Adv. Funct. Mater. 27 (2017) 1604262.

[3] X. Chen, Y. Song, Z. Su, H. Chen, X. Cheng, J. Zhang, M. Han, H. Zhang, Nano Energy 38 (2017) 43.

Accepted manuscript

ACCEPTED MANUSCRIPT

[4] B.K. Yun, H.S. Kim, Y.J. Ko, G. Murillo, J.H. Jung, Nano Energy 36 (2017) 233.

[5] L. Zhang, B. Zhang, J. Chen, L. Jin, W. Deng, J. Tang, H. Zhang, H. Pan, M. Zhu, W. Yang, Z. L. Wang, Adv. Mater. 28 (2016) 18120.

[6] L. Persano, C. Dagdeviren, Y. Su, Y. Zhang, S. Girardo, D. Pisignano, Y. Huang, J.A. Rogers, Nat. Commun. 4 (2013) 1633.

[7] D.A. Wang, K.H. Chang, Microelectronics Journal 41 (6) (2010) 356.

[8] M. Lallart, S. Pruvost, D. Guyomar, Phys. Lett. A 375 (45) (2011) 3921.

[9] K.Y. Lee, D. K, J.-H. Lee, T.Y. Kim, M.K. Gupta, S.-W. Kim, Adv. Funct. Mater. 24 (2014) 37.

[10] S.Y. Xu, Y.W. Yeh, G. Poirier, M.C. McAlpine, R.A. Register, N. Yao, Nano Lett. 13 (2013) 2393.

[11] L. Gu, N. Cui, L. Cheng, Q. Xu, S. Bai, M. Yuan, W. Wu, J. Liu, Y. Zhao, F. Ma, Y. Qin, Z.L. Wang, Nano Lett. 13 (2013) 91.

[12] G. Zhu, A.C. Wang, Y. Liu, Y. Zhou, Z.L. Wang, Nano Lett. 12 (2012) 3086.

[13] W. Qin, T. Li, Y. Li, J. Qiu, X. Ma, X. Chen, X. Hu, W. Zhang, Appl. Surf. Sci. 364 (2016) 670.

[14] J.M. Wu, C.C. Kao, RSC Adv. 4 (2014) 13882.

[15] J. Chen, S.K. Oh, H. Zou, S. Shervin, W. Wang, S. Pouladi, Y. Zi, Z.L. Wang, J. Ryou, ACS Appl. Mater. Interfaces 10 (2018) 12839.

[16] Y.F. Lin, J. Song, Y. Ding, S.-Y. Lu, Z.L. Wang, Appl. Phys. Lett. 92 (2008) 022105.

[17] E.J. Lee, T.Y. Kim, S.-W. Kim, S. Jeong, Y. Choi, S.Y. Lee, Energy Environ. Sci. 11 (2018) 1425.

[18] S.-H. Shin, Y.-H. Kim, M.H. Lee, J.-Y. Jung, J. Nah, ACS Nano 8 (2014) 2766.

Accepted manuscript

ACCEPTED MANUSCRIPT

[19] J.H. Jung, M. Lee, J. Hong, Y. Ding, C.-Y. Chen, L.-J. Chou, Z.L. Wang, ACS Nano 5 (2011) 10041.

[20] R. Guo, Y. Guo, H. Duan, H. Li, H. Liu, ACS Appl. Mater. Interfaces 9 (2017) 8271.

[21] S.N. Cha, S.M. Kim, H.J. Kim, J.Y. Ku, J.I. Sohn, Y.J. Park, B.G. Song, M.H. Jung, E.K. Lee, B.L. Choi, J.J. Park, Z.L. Wang, J.M. Kim, K. Kim, Nano Lett. 11 (2011) 5142.

[22] S. Park, Y. Kim, H. Jung, J.-Y. Park, N. Lee, Y. Seo, Sci. Rep. 7 (2017) 17290.

[23] S. Xu, B.J. Hansen, Z.L. Wang, Nat. Commun. 1 (2010) 93.

[24] C. Dagdeviren, B.D. Yang, Y.W. Su, P.L. Tran, P. Joe, E. Anderson, J. Xia, V. Doraiswamy, B. Dehdashti, X. Feng, B.W. Lu, R. Poston, Z. Khalpey, R. Ghaffari, Y.G. Huang, M.J. Slepian, J.A. Rogers, Proc. Natl. Acad. Sci. USA 111 (2014) 1927.

[25] J. Kwon, W. Seung, B.K. Sharma, S.W. Kim, J.H. Ahn, Energy Environ. Sci. 5 (2012) 8970.

[26] A.I. Kingon, S. Srinivasan, Nature Mater. 4 (2005) 233.

[27] Y. Qi, N.T. Jafferis, K. Lyons, C. M. Lee, H. Ahmad, M.C. McAlpine, Nano Lett. 10 (2010) 524.

[28] S.K. Karan, R. Bera, S. Paria, A.K. Das, S. Maiti, A. Maitra, B.B. Khatua, Adv. Energy Mater. 6 (2016) 1601016.

[29] J. Burschka, N. Pellet, S.J. Moon, R. Humphry-Baker, P. Gao, M.K. Nazeeruddin, M. Grätzel, Nature 499 (2013) 316.

[30] J. Seo, S. Park, Y. Chan Kim, N.J. Jeon, J.H. Noh, S.C. Yoon, S.I. Seok, Energy Environ. Sci. 7 (2014) 2642.

[31] N.J. Jeon, J.H. Noh, Y.C. Kim, W.S. Yang, S. Ryu, S.I. Seok, Nat. Mater. 13 (2014) 897.

Accepted manuscript

ACCEPTED MANUSCRIPT

[32] W.S. Yang, B.W. Park, E.H. Jung, N.J. Jeon, Y.C. Kim, D.U. Lee, S.S. Shin, J. Seo, E.K. Kim, J.H. Noh, Science 356 (2017) 1376.

[33] Y.-H. Kim, H. Cho, T.-W. Lee, Proc. Natl. Acad. Sci. U. S. A 113 (2016) 11694.

[34] M. Ahmadi, T. Wu, B. Hu, Adv. Mater. 29 (2017) 1605242.

[35] B.R. Sutherland, S. Hoogland, M.M. Adachi, C.T.O. Wong, E.H. Sargent, ACS Nano 8 (2014) 10947.

[36] J.S. Luo, Z. Li, S. Nishiwaki, M. Schreier, M.T. Mayer, P. Cendula, Y.H. Lee, K.W. Fu, A.Y. Cao, M.K. Nazeeruddin, Y.E. Ronmanyuk, S. Buecheler, S.D. Tilley, L.H. Wong, A.N. Tiwari, M. Gratzel, Adv. Energy Mater. 5 (2015) 1501520.

[37] S.P. Senanayak, B. Yang, T.H. Thomas, N. Giesbrecht, W. Huang, E. Gann, B. Nair, K. Goedel, S. Guha, X. Moya, C.R. McNeill, Sci. Adv. 3 (1) (2017) 1601935.

[38] E.J. Yoo, M. Lyu, J.H. Yun, C.J. Kang, Y.J. Choi, L. Wang, Adv. Mater. 27 (2015) 6170.

[39] Y.J. Kim, T.V. Dang, H.J. Choi, B.J. Park, J.H. Eom, H.A. Song, D. Seol, Y. Kim, S.H. Shin, H. Nah, S.-G. Yoon, J. Mater. Chem. A 4(2016) 756.

[40] C.C. Stoumpos, C.D. Malliakas, M.G. Kanatzidis, Inorg. Chem. 52 (2013) 9019.

[41] Y. Kutes, L. Ye, Y. Zhou, S. Pang, B.D. Huey, N.P. Padture, J. Phys. Chem. Lett. 5 (2014) 3335.

[42] M. Coll, A. Gomez, E. Mas-Marza, O. Almora, G. Garcia-Belmonte, M. Campoy-Quiles, J. Bisquert, J. Phys. Chem. Lett. 6 (2015) 1408.

[43] S. Liu, F. Zheng, I. Grinberg, A.M. Rappe, J. phys. Chem. Lett. 7 (2016) 1460.

[44] S. Ippili, V. Jella, J. Kim, S. Hong, S.-G. Yoon, Nano Energy 49 (2018) 247.

[45] V. Jella, S. Ippili, J.-H. Eom, Y.-J. Kim, H.-J. Kim, S.-G. Yoon, Nano Energy 52 (2018) 11.

Accepted manuscript

ACCEPTED MANUSCRIPT

[46] J. Zhang, X. Yang, H. Deng, K. Qiao, U. Farooq, M. Ishaq, F. Yi, H. Liu, J. Tang, H. Somg, Nano-Micro Lett. 9 (2017) 36.

[47] D. Wang, M. Wright, N.K. Elumalai, A. Uddin, Sol. Energy Mater. Sol. Cells 147 (2016) 255.

[48] V.M. Goldschmidt, Ber. Dtsch. Chem. Ges. 60 (1927) 1263.

[49] C. Li, X. Lu, W. Ding, L. Feng, Y. Gao, Z. Guo, Acta Crystallogr. B64 (2008) 702.

[50] N.-G. Park, Mater. Today 18 (2015) 65.

[51] M.K. Assadi, S. Bakhoda, R. Saidur, H. Hanaei, Renew. Sustain. Energy Rev. 81 (2017) 2812.

[52] M.A. Green, A. Ho-Baillie, H.J. Snaith, Nat. Photonics 8 (2014) 506.

[53] Z. Li, M. Yang, J.-S. Park, S.-H. Wei, J. Berry, K. Zhu, Chem. Mater. 28 (2016) 284.

[54] G. Kieslich, S. Sun, A.K. Cheetham, Chem. Sci. 5 (2014) 4712.

[55] B.N. Cohen, C. Labarca, N. Davidson, H.A. Lester, J. Gen. Physiol. 100 (1992) 373.

[56] A. Amat, E. Mosconi, E. Ronca, C. Quarti, P. Umari, M.K. Nazeeruddin, M. Grätzel, F. De Angelis, Nano Lett. 14 (2014) 3608.

[57] Q. Chen, N. De Marco, Y. Yang, T.-B. Song, C.-C. Chen, H. Zhao, Z. Hong, H. Zhou, Y. Yang, Nano Today 10 (2015) 355.

[58] C. Zheng, O. Rubel, J. Phys. Chem. C 121(22) (2017) 11977.

[59] Z. Fan, K. Sun, J. Wang, J. Mater. Chem. A 3 (2015) 18809.

[60] A. M. Glazer, Acta Crystallogr. Sect. B 28 (1972) 3384.

[61] K.P. Ong, T.W. Goh, Q. Xu, A. Huan, J. Phys. Chem. A 119 (2015) 11033.

[62] A. Dobrovolsky, A. Merdasa, E.L. Unger, A. Yartsev, I.G. Scheblykin, Nat. Commun. 8 (2017) 34.

Accepted manuscript

ACCEPTED MANUSCRIPT

[63] A. Maaej, M. Bahri, Y. Abid, N. Jaidane, Z.B. Lakhdar, A. Lautie, Phase Transitions 64 (1998) 179.

[64] A. Poglitsch, D. Weber, J. Chem. Phys. 87 (1987) 6373.

[65] K.-H. Wang, L.-C. Li, M. Shellaiah, K. Sun, Sci. Rep. 7 (2017) 13643.

[66] M.T. Klug, A. Osherov, A.A. Haghighirad, S.D. Stranks, P.R. Brown, S. Bai, J.T.-W. Wang, X. Dang, V. Bulović, H.J. Snaith, A.M. Belcher, Energy Environ. Sci. 10 (2017) 236.

[67] J.H. Noh, S.H. Im, J.H. Heo, T.N. Mandal, S.I. Seok, Nano Lett.13 (2013) 1764.

[68] J. Navas, A. Sánchez-Coronilla, J. J. Gallardo, N. Cruz Hernández, J.C. Piñero, R. Alcántara, C. Fernández-Lorenzo, D.M. De los Santos, T. Aguilar, J. Martín-Calleja, Nanoscale 7 (2015) 6216.

[69] J. Liu, G. Wang, Z. Song, X. He, K. Luo, Q. Ye, C. Liao, J. Mei, J. Mater. Chem. A 5 (2017) 9097.

[70] W. Ke, C.C. Stoumpos, I. Spanopoulos, L. Mao, M. Chen, M.R. Wasielewski, M.G. Kanatzidis, J. Am. Chem. Soc. 139 (2017) 14800.

[71] D. Sabba, H.K. Mulmudi, R.R. Prabhakar, T. Krishnamoorthy, T. Baikie, P.P. Boix, S.M haisalkar, N. Mathews, J. Phys. Chem. C 119 (2015) 1763.

[72] D. Ju, Y. Dang, Z. Zhu, H. Liu, C.-C. Chueh, X. Li, L. Wang, X. Hu, A.K.-Y. Jen, X. Ta o, Chem. Mater. 30 (2018) 1556.

[73] J. Berry, T. Buonassisi, D.A. Egger, G. Hodes, L. Kronik, Y.L. Loo, I. Lubomirsky, S.R. Marder, Y. Mastai, J.S. Miller, D.B. Mitzi, Y. Paz, A.M. Rappe, I. Riess, B. Rybtchinski, O. Stafsudd, V. Stevanovic, M.F. Toney, D. Zitoun, A. Kahn, D. Ginley, D. Cahen, Adv. Mater. 27 (2015) 5102.

Accepted manuscript

ACCEPTED MANUSCRIPT

[74] S.O. Kasap, Principles of electronic materials and devices. 3rd ed. (McGraw-Hill Education, New York, 2005).

[75] A.M.A. Leguy, J.M. Frost, A.P. McMahon, V.G. Sakai, W. Kochelmann, C.H. Law, X.E. Li, F. Foglia, A. Walsh, B.C. O'Regan, J. Nelson, J.T. Cabral, P.R.F. Barnes, Nat. Commun. 6 (2015) 10.

[76] J.M. Frost, K.T. Butler, F. Brivio, C.H. Hendon, M. van Schilfgaarde, A. Walsh, Nano Lett. 14 (2014) 2584.

[77] J.M. Frost, K.T. Butler, A. Walsh, APL Mater. 2 (2014) 081506.

[78] Z. Yang, A. Surrente, K. Galkowski, N. Bruyant, D.K. Maude, A.A. Haghighirad, H.J. Snaith, P. Plochocka, R.J. Nicholas, J. Phys. Chem. Lett. 8 (2017) 1851.

[79] T.-Y. Yang, G. Gregori, N. Pellet, M. Grätzel, J. Maier, Angew. Chem. Int. Ed. 54 (2015) 7905.

[80] Q.Q. Lin, A. Armin, R.C.R. Nagiri, P.L. Burn, P. Meredith, Nat. Photonics 9 (2015) 106.

[81] Y. Rakita, O. Bar-Elli, E. Meirzadeh, H. Kaslasi, Y. Peleg, G. Hodes, I. Lubomirsky, D. Oron, D. Ehre, D. Cahen, Proc. Natl. Acad. Sci. U. S. A 114 (2017) E5504.

[82] M. Hu, C. Bi, Y. Yuan, Z. Xiao, Q. Dong, Y. Shao, J. Huang, Small 11 (2015) 2164.

[83] F. Brivio, K.T. Butler, A. Walsh, M. van Schilfgaarde, Phys. Rev. B 89 (2014) 155204.

[84] J.M. Frost, A. Walsh, Acc. Chem. Res. 49 (2016) 528.

[85] A. Walsh, J. Phys. Chem. C 119 (2015) 5755.

[86] N. Onoda-Yamaura, T. Matsuo, H. Suga, J. Phys. Chem. Solids 53 (1992) 935.

[87] M. Maeda, M. Hattori, A. Hotta, I. Suzuki, J. Phys. Soc. Jpn. 66 (1997) 1508.

[88] M. Kato, T. Fujiseki, T. Miyadera, T. Sugita, S. Fujimoto, M. Tamakoshi, M. Chikamatsu, H. Fujiwara, J. Appl. Phys. 121 (2017) 115501.

Accepted manuscript

ACCEPTED MANUSCRIPT

[89] A.Yang, M. Bai, X. Bao, J. Wang, W. Zhang, J. Nanomed. Nanotechnol. 7 (5) (2016) 1000407.

[90] M.S. Alias, I. Dursun, M.I. Saidaminov, E.M. Diallo, P. Mishra, T.K. Ng, O.M. Bakr, B.S. Ooi, Opt. Express 24 (2016) 16586.

[91] M. Sendner, P.K. Nayak, D.A. Egger, S. Beck, C. Müller, B. Epding, W. Kowalsky, L. Kronik, H.J. Snaith, A. Pucci, R. Lovrincic, Mater. Horiz. 3 (2016) 613.

[92] J.M. Ball, S.D. Stranks, M.T. Hörantner, S. Hüttner, W. Zhang, E.J.W. Crossland, I. Ramirez, M. Riede, M.B. Johnston, R.H. Friend, Energy Environ. Sci. 8 (2015) 602.

[93] S. Govinda, B.P. Kore, M. Bokdam, P. Mahale, A. Kumar, S. Pal, B. Bhattacharyya, J. Lahnsteiner, G. Kresse, C. Franchini, A. Pandey, D.D. Sarma, J. Phys. Chem. Lett. 8 (2017) 4113.

[94] E.J. Juarez-Perez, R.S. Sanchez, L. Badia, G. Garcia-Belmonte, Y.S. Kang, I. Mora-Sero, J. Bisquert, J. Phys. Chem. Lett. 5 (2014) 2390.

[95] H. Ye, Y. Zhang, D. Fu, R. Xiong, Angew. Chem. Int. Ed. 53 (2014) 11242.

[96] W.-Q. Liao, Y. Zhang, C.-L. Hu, J.-G. Mao, H.-Y. Ye, P.-F. Li, S.D. Huang, R.-G. Xiong, Nat. Commun. 6 (2015) 7338.

[97] Y.-M. You, W.-Q. Liao, D. Zhao, H.-Y. Ye, Y. Zhang, Q. Zhou, X. Niu, J. Wang, P.-F. Li, D.-W. Fu, Z. Wang, S. Gao, K. Yang, J.-M. Liu, J. Li, Y. Yan, R.-G. Xiong, Science 357 (2017) 306.

[98] A. García-Fernández, J.M. Bermúdez-García, S. Castro-García, A.L. Llamas-Saiz, R. Artiaga, J. López-Beceiro, S. Hu, W. Ren, A. Stroppa, M. Sánchez-Andújar, M.A. Señarís-Rodríguez, Inorg. Chem. 56 (2017) 4918.

Accepted manuscript

ACCEPTED MANUSCRIPT

[99] J. Dhar, S. Sil, N.A. Hoque, A. Dey, S. Das, P.P. Ray, D. Sanyal, ChemistrySelect 3 (2018) 5304.

[100] V. Jella, S. Ippili, J.-H. Eom, J. Choi, S.-G. Yoon, Nano Energy 53 (2018) 46.

[101] R. Ding, H. Liu, X. Zhang, J. Xiao, R. Kishor, H. Sun, B. Zhu, G. Chen, F. Gao, X. Feng, J. Chen, X. Chen, X. Sun, Y. Zheng, Adv. Funct. Mater. 26 (2016) 7708.

[102] H. Hammami, M. Arous, M. Lagache, A. Kallel, Composites Part A. 37 (2006) 1.

[103] H. Hammami, M. Arous, M. Lagache, A. Kallel, J. Alloys Compd. 430 (2007) 1.

[104] J. Anjana, K.J. Prashanth, Kr.S. Asheesh, J. Arpit, P.N. Rashmi, Polym. Eng. Sci. 55(2015) 1589.

[105] R. Fries, A.J. Moulson, J. Mater. Sci. 5 (1994) 238.

[106] Y.J. Choi, M.J. Yoo, H.W. Kang, H.G. Lee, S.H. Han, S. Nahm, J. Electroceram. 30 (2013) 30.

[107] B. Chen, M. Yang, S. Priya, K. Zhu, J. Phys. Chem. Lett. 7 (2016) 905.

[108] F. Zheng, H. Takenaka, F. Wang, N.Z. Koocher, A.M. Rappe, J. Phys. Chem. Let. 6 (201 4) 31.

[109] H.S. Kim, S.K. Kim, B.J. Kim, K.S. Shin, M.K. Gupta, H.S. Jung, S.W. Kim, N.G. Park, J. Phys. Chem. Lett., 6 (2015) 1729.

[110] H. Röhm, T. Leonhard, M.J. Hoffmann, A. Colsmann, Energy Environ. Sci. 10 (2017) 95 0.

[111] F. Bi, S. Markov, R. Wang, Y.H. Kwok, W. Zhou, L. Liu, X. Zheng, G.H. Chen, C.Y. Ya m, J. Phys. Chem. C 121 (2017) 11151.

[112] C. Quarti, E. Mosconi, F. De Angelis, Chem. Mater. 26 (2014) 6557.

[113] Z. Fan, J. Xiao, K. Sun, L. Chen, Y. Hu, J. Ouyang, K.P. Ong, K. Zeng, J. Wang, J. Phys.

Accepted manuscript

ACCEPTED MANUSCRIPT

Chem. Lett. 6 (2015) 1155.

[114] D. Seol, A. Jeong, M.H. Han, S. Seo, T.S. Yoo, W.S. Choi, H.S. Jung, H. Shin, Y. Kim, Adv. Funct. Mater. 5 (2017) 1701924.

[115] M.M. Alam, S.K. Ghosh, A. Sultana, D. Mandal, Nanotechnology 26 (2015) 165403.

[116] A. Labuda, R. Proksch, Appl. Phys. Lett. 106 (2015) 253103.

[117] S.V. Kalinin, A. Kumar, N. Balke, M.L. McCorkle, S. Guo, T.M. Arruda, S. Jesse, Adv. Mater. Process 169 (2011) 30.

[118] N. Balke, P. Maksymovych, S. Jesse, I.I. Kravchenko, Q. Li, S.V. Kalinin, ACS Nano 8 (2014) 10229.

[119] S.V. Kalinin, S. Jesse, A. Tselev, A.P. Baddorf, N. Balke, ACS Nano 5 (2011) 5683.

[120] Q. Dong, J. Song, Y. Fang, Y. Shao, S. Ducharme, J. Huang, Adv. Mater. 28 (2016) 2816.

[121] J. Song, Z. Xiao, B. Chen, S. Prockish, X. Chen, A. Rajapitamahuni, L. Zhang, J. Huang, X. Hong, ACS Appl. Mater. Interfaces 10 (2018) 19218.

[122] S. Huang, G. Tang, H. Huang, X.-G. Wu, P. Zhou, L. Zou, L. Xie, J. Deng, X. Wang, H. Zhong, J. Hong, Sci. Bull. 63 (2018) 1254.

[123] K. Sakayori, Y. Matsui, H. Abe, E. Nakamura, M. Kenmoku, T. Hara, D. Ishikawa, A. Kokubu, K. Hirota, T. Ikeda, Jpn J. Appl. Phys. 34 (1995) 5443.

[124] H. Zhou, Q. Chen, G. Li, S. Luo, T.-b. Song, H.-S. Duan, Z. Hong, J. You, Y. Liu, Y. Yang, Science 345 (2014) 542.

[125] J.H. Heo, H.J. Han, D. Kim, T.K. Ahn, S.H. Im, Energy Environ. Sci. 8 (2015) 1602.

[126] X. Hu, X. Zhang, L. Liang, J. Bao, S. Li, W. Yang, Y. Xie, Adv. Funct. Mater. 24 (2014) 7373.

Accepted manuscript

ACCEPTED MANUSCRIPT

[127] J.-H. Im, I.-H. Jang, N. Pellet, M. Grätzel, N.-G. Park, Nat. Nanotechnol. 9 (2014) 927.

[128] Z. Xiao, C. Bi, Y. Shao, Q. Dong, Q. Wang, Y. Yuan, C. Wang, Y. Gao, J. Huang, Energy Environ. Sci. 7 (2014) 2619.

[129] Y. Xu, L. Zhu, J. Shi, S. Lv, X. Xu, J. Xiao, J. Dong, H. Wu, Y. Luo, D. Li, Q. Meng, ACS Appl. Mater. Interfaces 7 (2015) 2242.

[130] M. Jiang, J. Wu, F. Lan, Q. Tao, D. Gao, G. Li, J. Mater. Chem. A 3 (2015) 963.

[131] M. Xiao, F.Z. Huang, W. Huang, Y. Dkhissi, Y. Zhu, J. Etheridge, A. Gray-Weale, U. Bach, Y.-B. Cheng, L. Spiccia, Angew. Chem. Int. Ed. 53 (2014) 9898.

[132] Y. Deng, X. Zheng, Y. Bai, Q. Wang, J. Zhao, J. Huang, Nat. Energy 3 (2018) 560.

[133] J.E. Bishop, T.J. Routledge, D.G. Lidzey, J. Phys. Chem. Lett. 9 (2018) 1977.

[134] M. Liu, M.B. Johnston, H.J. Snaith, Nature 501 (2013) 395.

[135] M.R. Leyden, L.K. Ono, S.R. Raga, Y. Kato, S. Wang, Y. Qi, J. Mater. Chem. A 2 (2014) 18742.

[136] M.R. Leyden, M.V. Lee, S.R. Ragaa, Y. Qi, J. Mater. Chem. A 3 (2015) 16097.

[137] Q. Chen, H. Zhou, Z. Hong, S. Luo, H.-S. Duan, H.-H. Wang, Y. Liu, G. Li, Y. Yang, J. Am. Chem. Soc. 136 (2014) 622.

[138] F. Zhang, H. Zhong, C. Chen, X.-G. Wu, X. Hu, H. Huang, J. Han, B. Zou, Y. Dong, ACS Nano 9 (2015) 4533.

[139] R. Pan, H. Li, J. Wang, X. Jin, Q. Li, Z. Wu, J. Gou, Y. Jiang, Y. Song, Part. Part. Syst. Charact. 35 (2018) 1700304.

[140] H. Huang, A.S. Susha, S.V. Kershaw, T.F. Hung, A.L. Rogach, Adv. Sci. 2 (2015) 1500194.

[141] C.H. Lu, J. Hu, W.Y. Shih, W.H. Shih, J. Colloid Interface Sci. 484 (2016) 17.

Accepted manuscript

ACCEPTED MANUSCRIPT

[142] A. Kirakosyan, J. Kim, S.W. Lee, I. Swathi, S.-G. Yoon, J. Choi, Cryst. Growth Des. 17 (2017) 794.

[143] P. Arunkumar, K. Gil, S. Won, S. Unithrattil, Y. Kim, H. Kim, W. Im, J. Phys. Chem. Lett. 8 (2017) 4161.

[144] X. Li, Y. Wu, S. Zhang, B. Cai, Y. Gu, J. Song, H. Zeng, Adv. Funct. Mater. 26 (2016) 2435.

[145] S.B. Sun, D. Yuan, Y. Xu, A.F. Wang, Z.T. Deng, ACS Nano 10 (2016) 3648.

[146] L. Protesescu, S. Yakunin, M.I. Bodnarchuk, F. Krieg, R. Caputo, C.H. Hendon, R.X. Yang, A. Walsh, M.V. Kovalenko, Nano Lett. 15 (2015) 3692.

[147] H. Huang, F. Zhao, L. Liu, F. Zhang, X.-G. Wu, L. Shi, B. Zou, Q. Pei, H. Zhong, ACS Appl. Mater. Interfaces 7 (2015) 28128.

[148] D.M. Jang, D.H. Kim, K. Park, J. Park, J.W. Lee, J.K. Song, J. Mater. Chem. C 4 (2016) 10625.

[149] Y. Kesari, A. Athawale, Mater. Lett. 159 (2015) 87.

[150] V.B. Kumar, L. Gouda, Z.e. Porat, A. Gedanken, Ultrason. Sonochem. 32 (2016) 54.

[151] G.C. Papavassiliou, G.A. Mousdis, G.A. Anyfantis, Luminescence 25 (2010) 218.

[152] K. Manukyan, A. Yeghishyan, D. Moskovskikh, J. Kapaldo, A. Mintairov, A. Mukasyan, J. Mat. Sci. 51(2016) 9123.

[153] P. Sadhukhan, S. Kundu, A. Roy, A. Ray, P. Maji, H. Dutta, S.K. Pradhan, S. Das, Cryst. Growth Des. 18 (2018) 3428.

[154] V.A. Hintermayr, A.F. Richter, F. Ehrat, M. Doblinger, W. Vanderlinden, J.A. Sichert, Y. Tong, L. Polavarapu, J. Feldmann, A.S. Urban, Adv. Mater. 28 (2016) 9478.

Accepted manuscript

ACCEPTED MANUSCRIPT

[155] H. Huang, Q. Xue, B. Chen, Y. Xiong, J. Schneider, C. Zhi, H. Zhong, A.L. Rogach, Angew. Chem. Int. Ed. 56 (2017) 9571.

[156] S. Yun, A. Kirakosyan, S.-G. Yoon, J. Choi, ACS Sustainable Chem. Eng. 6 (2018) 3733.

[157] T. Hanemann, D.V. Szabo, Materials 3 (2010) 3468.

[158] A. Pan, J. Wang, M.J. Jurow, M. Jia, Y. Liu, Y. Wu, Y. Zhang, L. He, Y. Liu, Chem. Mater. 30 (2018) 2771.

[159] S. Masi, S. Colella, A. Listorti, V. Roiati, A. Liscio, V. Palermo, A. Rizzo, G. Gigli, Sci. Rep. 5 (2015) 7725.

[160] H. Wang, Y. Rahaq, V. Kumar, Sci. Rep. 6 (2016) 29567.

[161] A. Privitera, M. Righetto, M. De Bastiani, F. Carraro, M. Rancan, L. Armelao, G. Granozzi, R. Bozio, L. Franco, J. Phys. Chem. Lett. 8 (2017) 5981.

[162] Z.L. Wang, J.H. Song, Science 312 (2006) 242.

[163] J.H. Eom, H. J. Choi, S.V.N. Pammi, V.D. Tran, Y.J. Kim, H.J. Kim, S.-G. Yoon, J. Mater. Chem. C 6 (2018) 2786.

[164] K.-I. Park, J.H. Son, G.-T. Hwang, C.K. Jeong, J. Ryu, M. Koo, I. Choi, S.H. Lee, M. Byun, Z.L. Wang, K.J. Lee, Adv. Mater. 26 (2014) 2514.

[165] X. Chen, S. Xu, N. Yao, Y. Shi, Nano Lett. 10 (2010) 2133.

[166] S. S. Won, M. Sheldon, N. Mostovych, J. Kwak, B.-S. Chang, C. W. Ahn, A. I. Kingon, I. W. Kim and S.-H. Kim, Appl. Phys. Lett. 107 (2015) 202901.

[167] Q. Zheng, H. Zhang, H. Mi, Z. Cai, Z. Ma, S. Gong, Nano Energy 26 (2016) 504.

[168] Y. Wang, M. Fang, B. Tian, P. Xiang, N. Zhong, H. Lin, C. Luo, H. Peng, C.- G. Duan, ChemistrySelect 2 (2017) 7951.

Accepted manuscript

ACCEPTED MANUSCRIPT

[169] A. Sultana, S.K. Ghosh, V. Sencadas, T. Zheng, M.J. Higgins, T.R. Middya, D. Mandal, J. Mater. Chem. B 5 (2017) 7352.

[170] J. Chun, N.-R. Kang, J.-Y. Kim, M.-S. Noh, C.-Y. Kang, D. Choi, S.-W. Kim, Z.L. Wang, J.M. Baik, Nano Energy 11 (2015) 1.

[171] A. Sultana, M.M. Alam, S. Garain, T.K. Sinha, T.R. Middya, D. Mandal, ACS Appl. Mater. Interfaces 7 (2015) 19091.

[172] N.R. Alluri, B. Saravanakumar, S.J. Kim, ACS Appl. Mater. Interfaces 7 (2015) 9831.

[173] K.I. Park, M.B. Lee, Y. Liu, S. Moon, G.T. Hwang, G. Zhu, J.E. Kim, S.O. Kim, D.K. Kim, Z.L. Wang, K.J. Lee, Adv. Mater. 24 (2012) 2999.

[174] K. I. Park, C. K. Jeong, J. Ryu, G. T. Hwang, K. J. Lee, Adv. Energy Mater. 3 (2013) 1539.

[175] R. Ding, X. Zhang, G. Chen, H. Wang, R. Kishor, J. Xiao, F. Gao, K. Zeng, X. Chen, X.W. Sun, Y. Zheng, Nano Energy 37 (2017) 126.

[176] A. Sultana, P. Sadhukhan, M.M. Alam, S. Das, T.R. Middya, D. Mandal, ACS Appl. Mater. Interfaces 10 (2018) 4121.

[177] A. Sultana, M. M. Alam, P. Sadhukhan, U.K. Ghorai, S. Das, T.R. Middya, D. Mandal, Nano Energy 49 (2018) 380.

Accepted manuscript

ACCEPTED MANUSCRIPT

Figure 1 (a) Crystal structure of ABX_3 perovskite. Reproduced with permission [47]. Copyright 2016, Elsevier. (b) Calculated octahedral and tolerance factors for different commonly used organic and inorganic hybrid perovskite compounds. Reproduced with permission [57]. Copyright 2015, Elsevier.

Figure 2 The frequency dependence of the real and imaginary parts of the dielectric constants in the presence of interfacial/space charge, orientational, ionic, and electronic polarization mechanisms [74].

Figure 3 Temperature-dependent dielectric constant of $MAPbI_3$ for (a) orthorhombic-tetragonal phase transition, reproduced with permission [93]. Copyright 2015, American Chemical Society. and (b) tetragonal-cubic phase transition. Reproduced with permission [39]. Copyright 2015, The Royal Society of Chemistry. The inset in (a) shows the fit to the experimental data of the dielectric constant *vs.* temperature in the tetragonal phase of $MAPbI_3$. (c) Tetragonal-cubic phase transition of Fe^{2+}-incorporated $MAPbI_3$ with various volume fractions of Fe^{2+} measured at 100 kHz. Reproduced with permission [44]. Copyright 2018, Elsevier. (d) Dielectric constant and dissipation factor of $MAPbI_3$-PVDF composite films with different volume fractions of $MAPbI_3$ at 1 kHz. Reproduced with permission [100]. Copyright 2018, Elsevier.

Figure 4 (a) AFM topography images (top row), and corresponding underneath PFM images mapping the $A \cdot \sin(\varphi)$ piezoresponse after DC poling, indicating the partial reversible ferroelectric domain switching after different biasing processes for β-$MAPbI_3$ films. Reproduced with permission [41]. Copyright 2014, American Chemical Society. Ferroelectric domain structures of TMCM-$MnCl_3$ observed in the (b) phase and (c) amplitude PFM images of the out-

Accepted manuscript

ACCEPTED MANUSCRIPT

of-plane piezoresponse. (b, c) Reproduced with permission [97]. Copyright 2017, The American Association for the Advancement of Science.

Figure 5 (a) Deflection *vs.* V_{AC} measured at room temperature (black circle), 40 ºC (blue open circles) in dark, and under illumination (pink triangles) at room temperature for $MAPbI_3$ films. Reproduced with permission [42]. Copyright 2015, American Chemical Society. (b) Piezoelectric coefficient of a $MAPbI_3$ single crystal from a plot of the intensity modulation ΔI vs. amplitude of a 1 kHz ac electric field applied across the crystal. Reproduced with permission [120]. Copyright 2016, Wiley-VCH. (c) Schematic diagram of the sample for PFM measurement and plot represents d_{33} vs. t_{MA} for $MAPbI_3$ on PZT, Au, ITO and STO. Reproduced with permission [121]. Copyright 2018, American Chemical Society. (d) Schematic illustration of the molecular ordering of $MAPbI_3$ under illumination and its light-enhanced piezoelectricity. Reproduced with permission [43]. Copyright 2016, American Chemical Society. (e) Piezoelectric coefficient (d_{33}) of TMCM-$MnCl_3$ as a function of temperature; the inset shows the frequency-dependent piezoelectric coefficient. (f) Comparison of the piezoelectric coefficients of inorganic and molecular materials with TMCM-$MnCl_3$. (e, f) Reproduced with permission [97]. Copyright 2017, The American Association for the Advancement of Science.

Figure 6 Schematic illustrations of the representative synthetic approaches for perovskite polycrystalline films. (a) One-step solution process of $MAPbI_3$ by a mixture of PbI_2 and MAI dissolved in DMF. (b) Two-step sequential coating of PbI_2 and MAI to form $MAPbI_3$. Reproduced with permission [127]. Copyright 2014, Springer Nature. (c) Two-step sequential coating of PbI_2 and MAI by combining spin-coating and dip-coating processes. (d) SEM images of $MAPbI_3$ film with various grain sizes depending on the concentration of the precursor solution. Reproduced with permission [127]. Copyright 2014, Springer Nature. (e) fast-

Accepted manuscript

ACCEPTED MANUSCRIPT

deposition crystallization technique to fabricate $MAPbI_3$ thin film using a poor solvent (i.e. chlorobenzene) and the corresponding SEM images. Reproduced with permission [131]. Copyright 2014, Wiley-VCH. (f) Double-source vacuum evaporation using $PbCl_2$ and MAI sources. Reproduced with permission [134]. Copyright 2013, Springer Nature. (g) two-step chemical vapor-assisted process using MAI organic vapor on PbI_2 films. Reproduced with permission [137]. Copyright 2014, American Chemical Society.

Figure 7 Schematic description of the representative synthetic process for low-dimensional OMHP nanocrystals. (a) LARP process and the TEM images of the resultant nanocrystals. Reproduced with permission [138]. Copyright 2015, American Chemical Society. (b) Non-aqueous emulsion synthesis and picture of nanocrystal powder. Reproduced with permission [147]. Copyright 2015, American Chemical Society. (c) Ultrasonication technique and TEM image of OMHP nanocrystals. Reproduced with permission [148]. Copyright 2016, The Royal Society of Chemistry. (d) 10 g of $MAPbBr_3$ nanocrystals produced by ligand-assisted ball-milling. Reproduced with permission [156]. Copyright 2018, American Chemical Society.

Figure 8 (a) Schematic representation of the power generation mechanism for a $MAPbI_3$ thin-film-based PEG. Reproduced with permission [39]. Copyright 2015, The Royal Society of Chemistry. (b, c) Schematic and photographs of fabricated Fe^{2+}-incorporated $MAPbI_3$ PEG, (d) comparison of output voltage and current density of a Fe^{2+}-incorporated $MAPbI_3$ PEG as a function of Fe^{2+} concentration, (e) captured images of instant lighting of LED during the application of mechanical pressure. (b-e) Reproduced with permission [44]. Copyright 2018, Elsevier. (f) Schematic diagram of $MAPbI_3$ deposition using a two-zone CVD system, (g) schematic illustration of a pressure and light-sensitive bimodal sensor of $MAPbI_3$, and (h)

Accepted manuscript

ACCEPTED MANUSCRIPT

sensitivity of the $MAPbI_3$ pressure sensor from a voltage *vs.* pressure plot. (f-h) Reproduced with permission [163]. Copyright 2018, The Royal Society of Chemistry.

Figure 9 (a) Fabrication steps, (b) captured digital image, and (c) captured optical images of an IDE-based $MAPbI_3$ PEG. (d) Schematic and SEM cross-sectional image of an IDE-based $MAPbI_3$ PEG. (e) Output voltage and current of an IDE-based $MAPbI_3$ PEG measured with an applied pressure of 0.2 MPa. (f) Schematic representation of an IDE-based $MAPbI_3$ PEG operating mechanism. (a-f) Reproduced with permission [45]. Copyright 2018, Elsevier.

Figure 10 (a, b**)** schematic diagram and SEM cross-sectional image of a fabricated $FAPbBr_3$-PDMS composite-based PEG, and (c) its measured output voltage. (a-c) Reproduced with permission [101]. Copyright 2016, Wiley-VCH. (d) FE-SEM image of a $MAPbI_3$ particle grinded for 15 min. (e, f) schematic and photograph of a fabricated $MAPbI_3$-PDMS composite PEG. (d-f) Reproduced with permission [99]. Copyright 2018, Wiley-VCH.

Figure 11 (a) Fabrication procedure for a $FAPbBr_3$-PVDF composite PEG, (b) SEM cross-sectional image of a fabricated PEG, and (c) its magnified cross-sectional image representing the distribution of $FAPbBr_3$ NPs in a PVDF polymer. (a-c) Reproduced with permission [175]. Copyright 2017, Elsevier. Schematic representation of (d) formation of the electroactive phase in a $MAPbI_3$-PVDF composite film and (e) fabrication of a $MAPbI_3$-PVDF composite film-based PEG, and (f) its measured output voltage. (d-f) Reproduced with permission [176]. Copyright 2018, American Chemical Society. (g) FE-SEM image of $MAPbBr_3$-PVDF composite electrospun fibers. The inset shows the corresponding fiber diameter distribution. (h) Output voltage of an acoustic nanogenerator-based $MAPbBr_3$-PVDF composite materials and (i) the

Accepted manuscript

ACCEPTED MANUSCRIPT

powering of a wristwatch by the charged capacitor using a $MAPbBr_3$-PVDF composite acoustic nanogenerator. (g-i) Reproduced with permission [177]. Copyright 2018, Elsevier.

Figure 12 (a) SEM-EDS surface mapping images of $MAPbI_3$-PVDF composite films, (b) schematic illustration of the working mechanism of a $MAPbI_3$-PVDF composite PEG, (c) schematic diagram of a $MAPbI_3$-PVDF composite PEG; the cross-sectional image denotes the thickness of the composite film. (d) Output voltage and current density of a $MAPbI_3$-PVDF PEG. (e, f) Captured images of the instant lighting of LEDs by rectified electric power under an applied pressure of 50 N and during finger tapping, respectively. (a-f) Reproduced with permission [100]. Copyright 2018, Elsevier.

Accepted manuscript

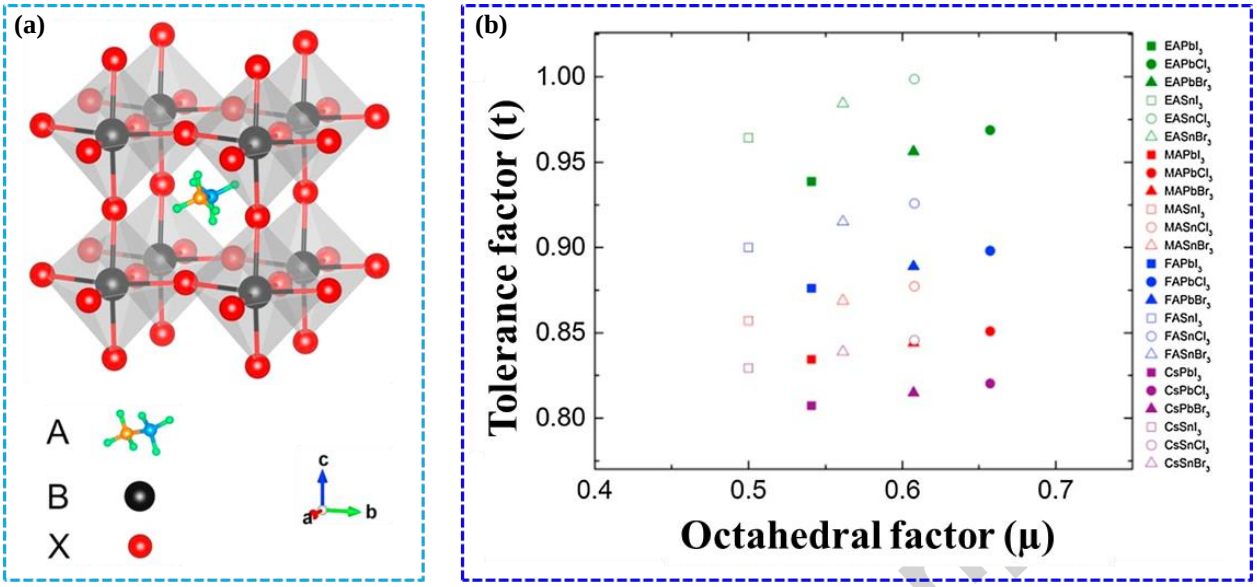

Fig.1 **Venkatraju et al.**

Accepted manuscript

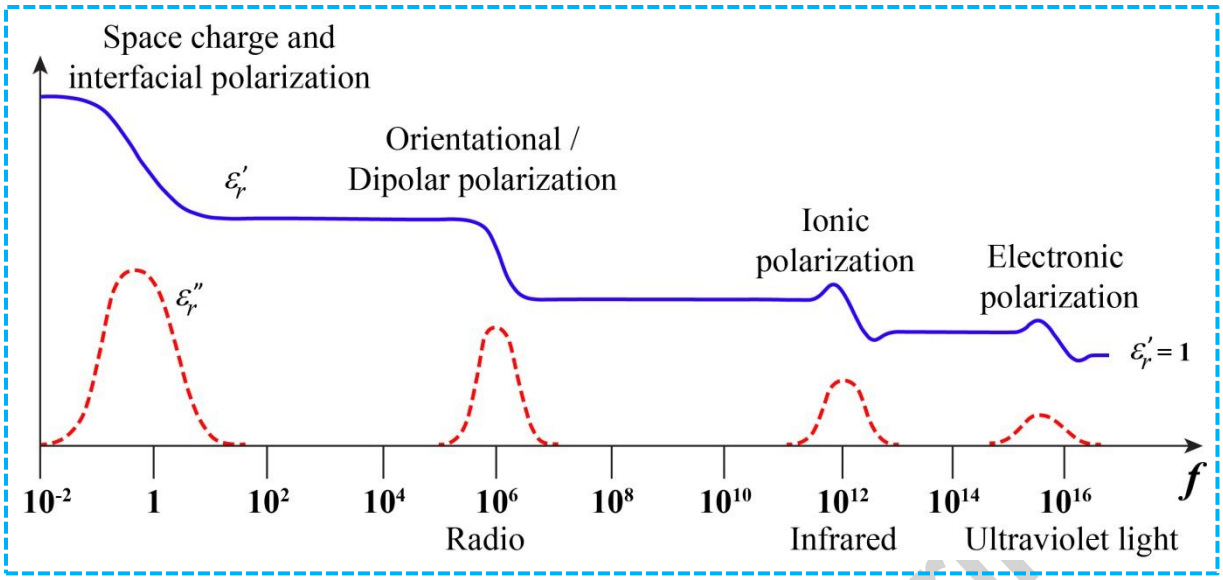

Fig.2 **Venkatraju et al.**

Accepted manuscript

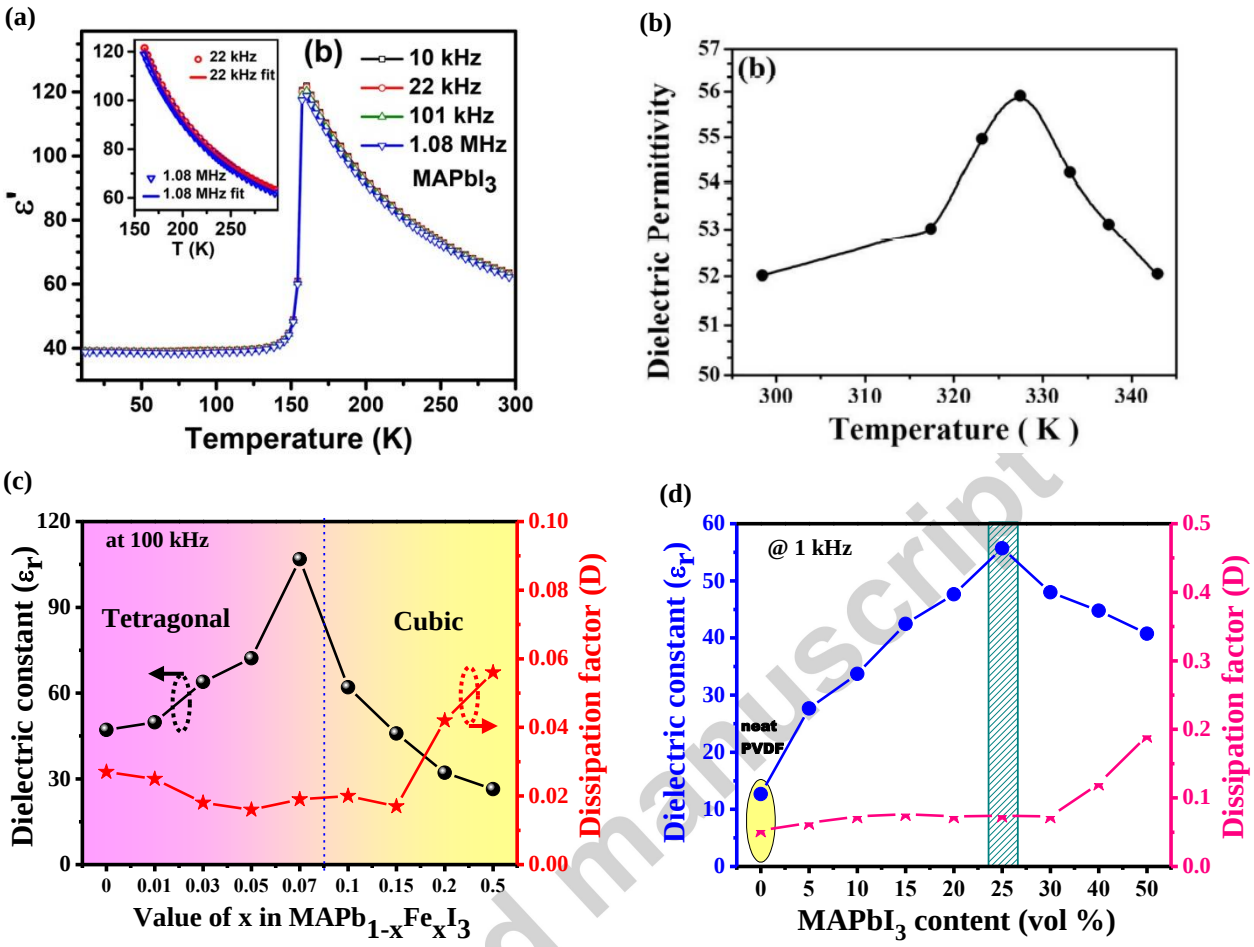

Fig.3 **Venkatraju et al.**

Accepted manuscript

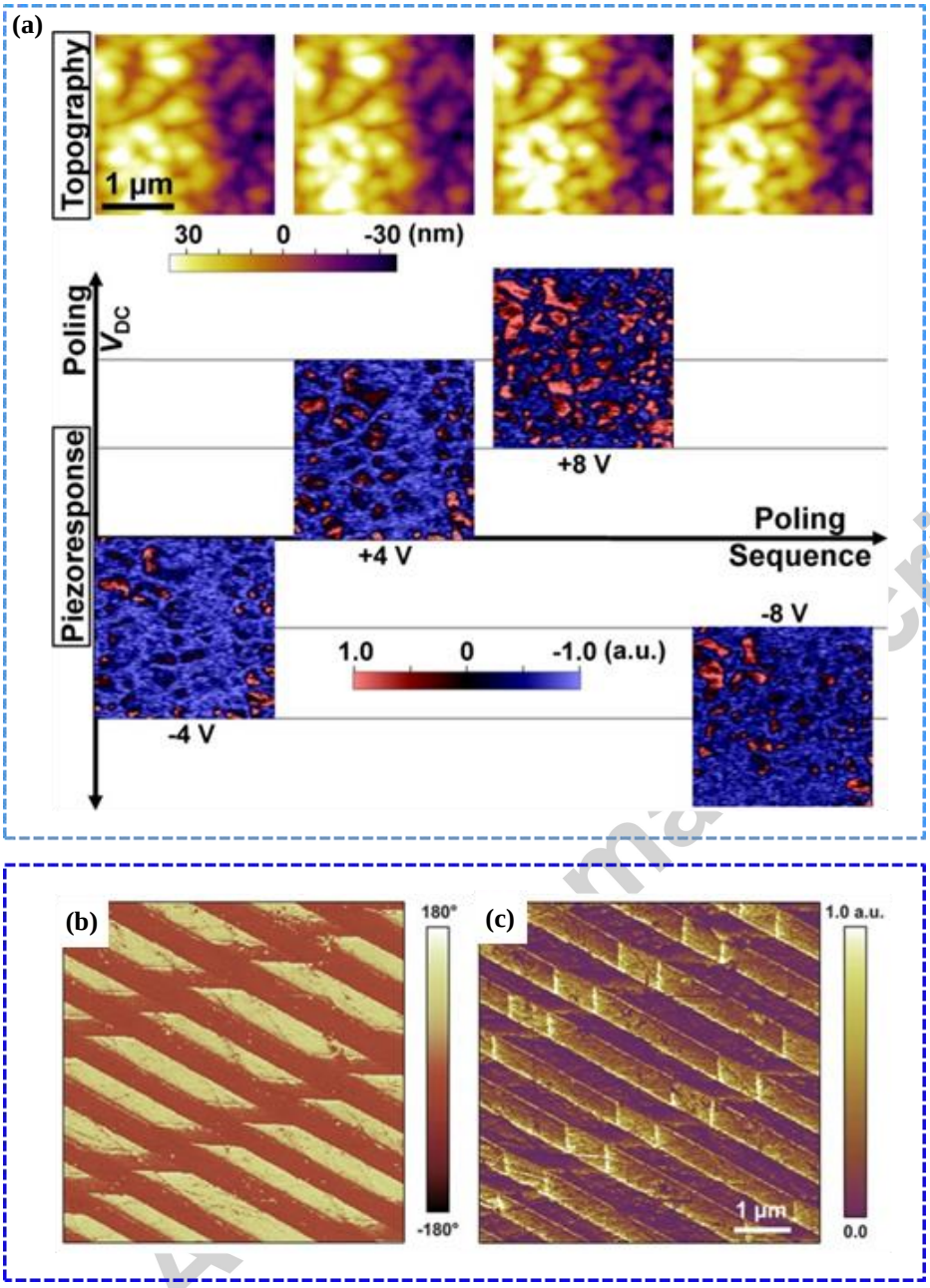

Fig.4 **Venkatraju et al.**

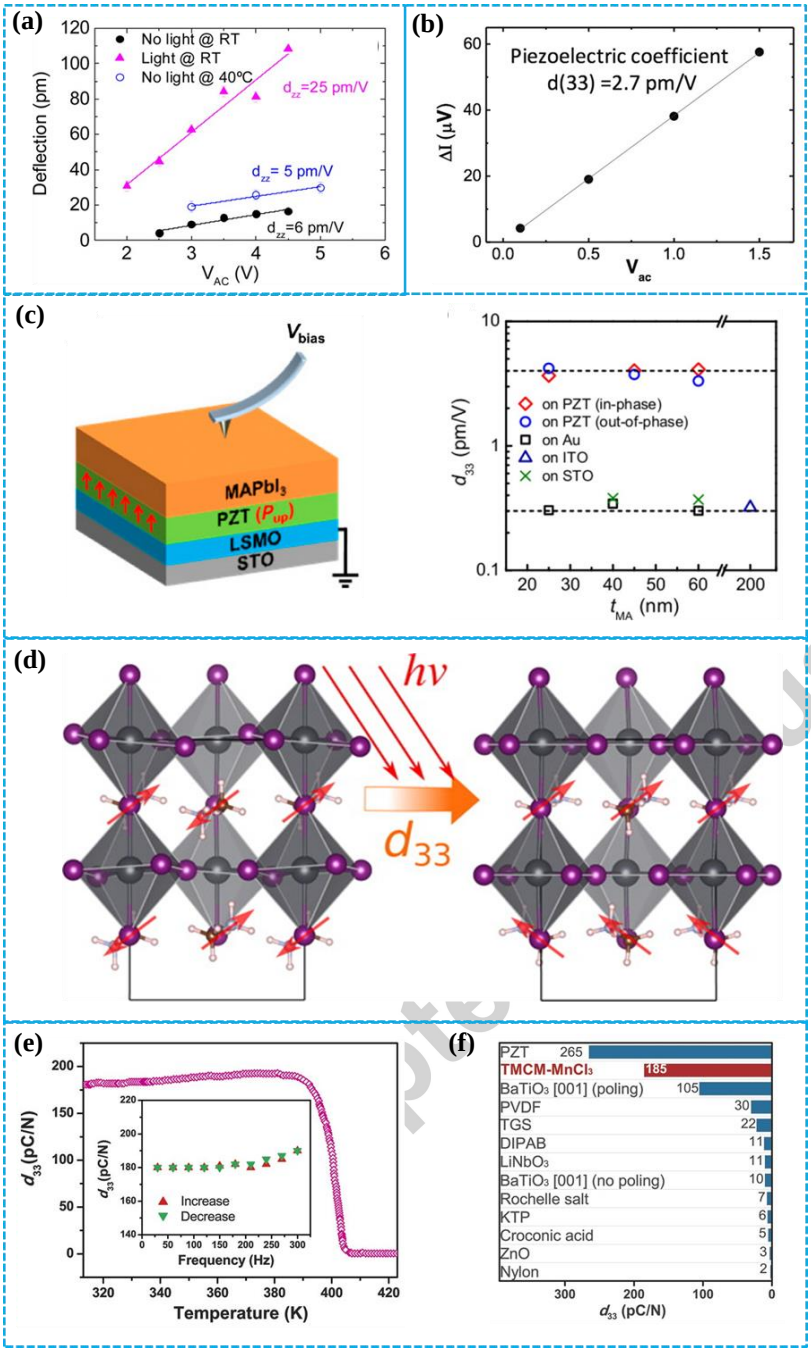

Fig.5 **Venkatraju et al.**

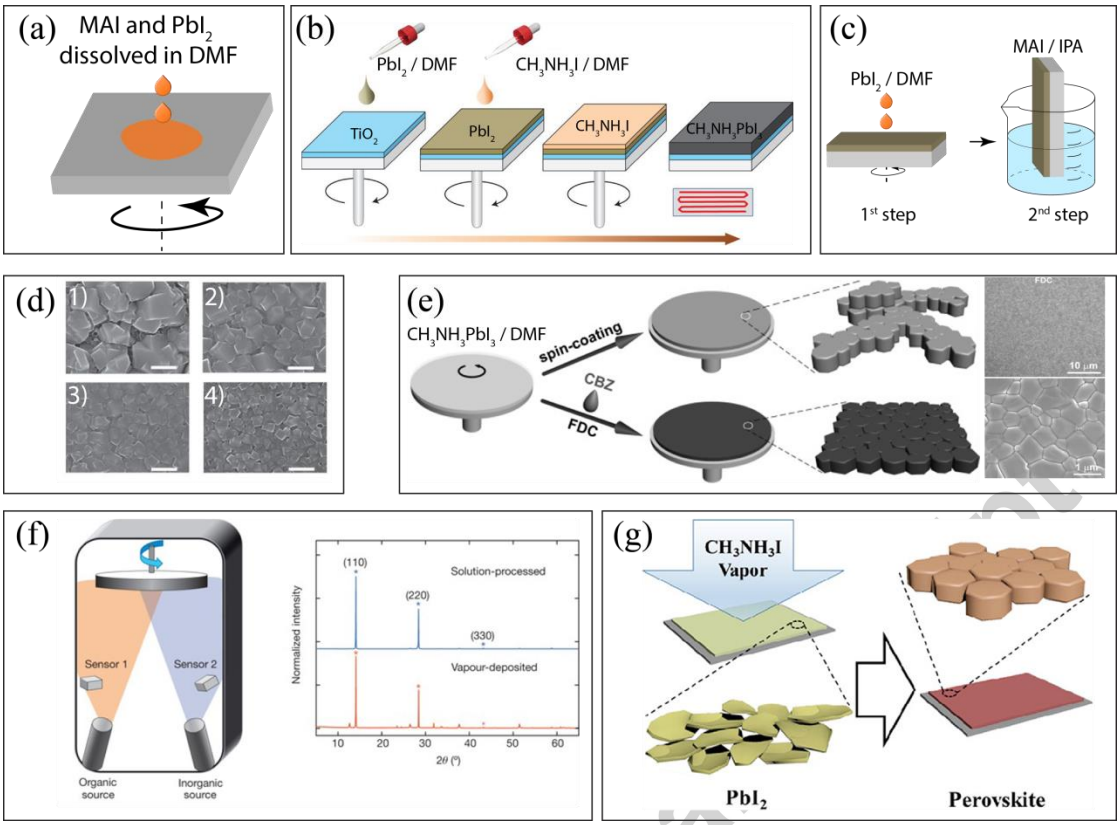

Fig.6 **Venkatraju et al.**

Accepted manuscript

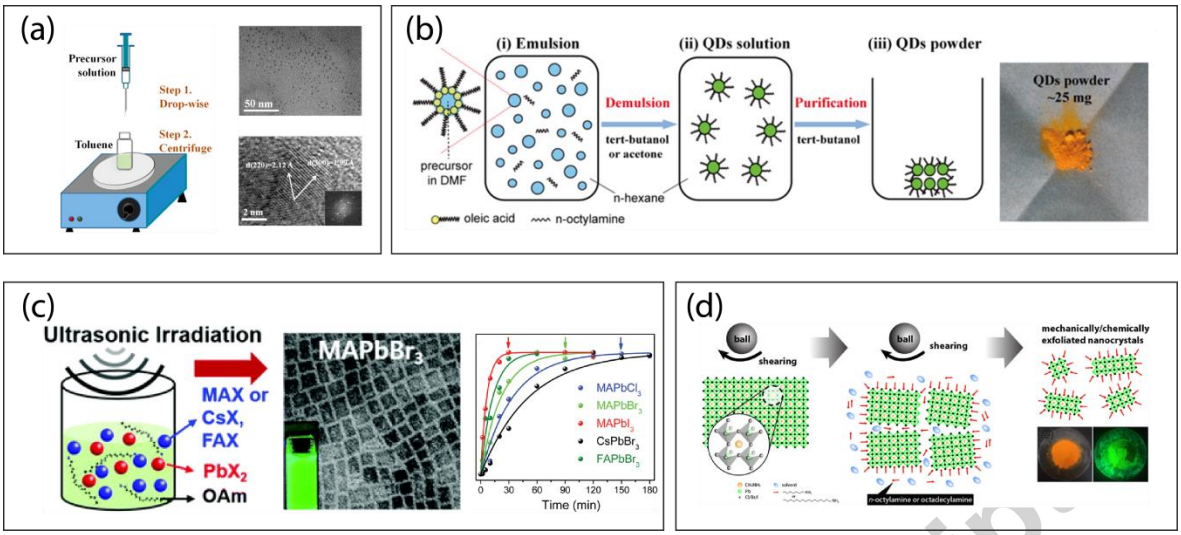

Fig.7 **Venkatraju et al.**

Accepted manuscript

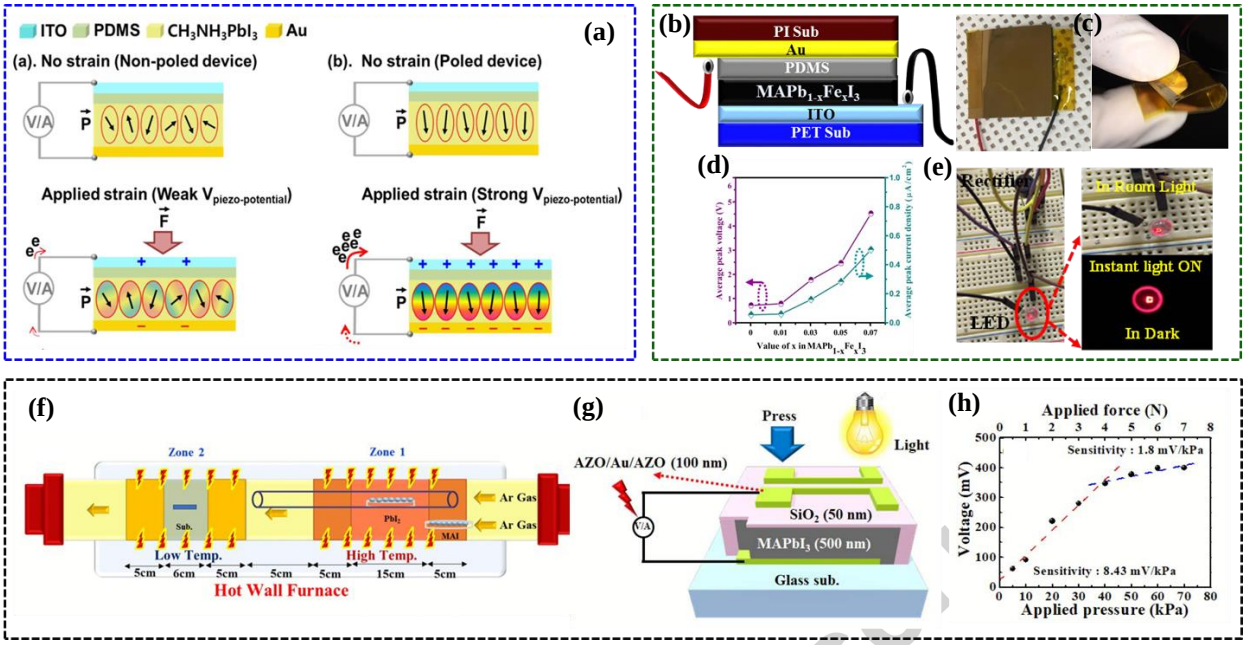

Fig.8 **Venkatraju et al.**

Accepted manuscript

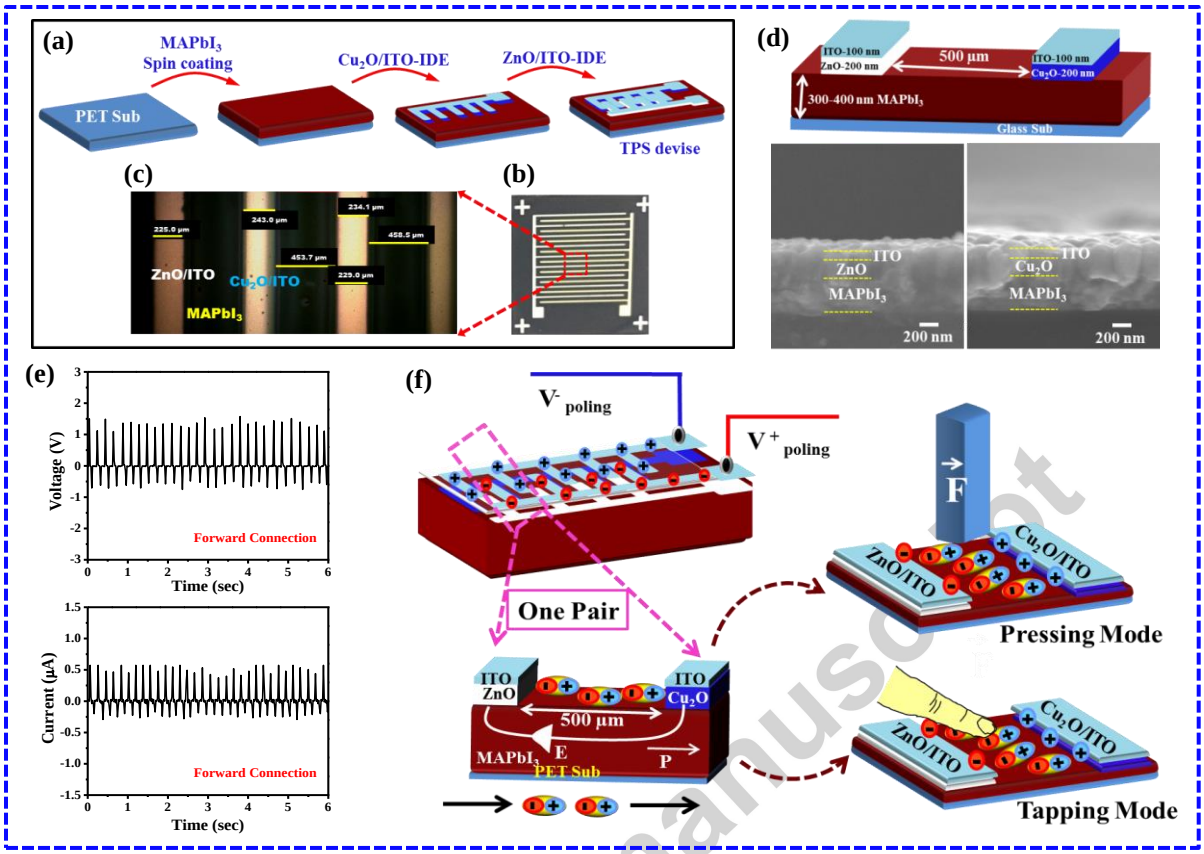

Fig.9 **Venkatraju et al.**

Accepted manuscript

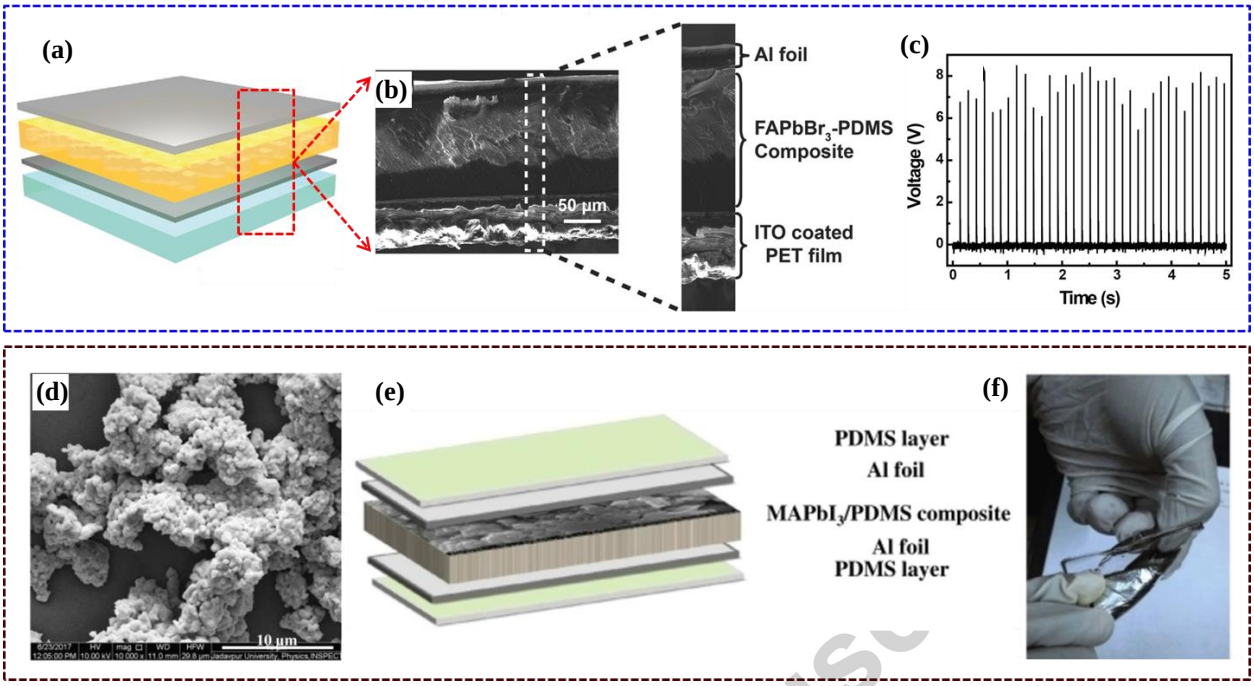

Fig.10 **Venkatraju et al.**

Accepted manuscript

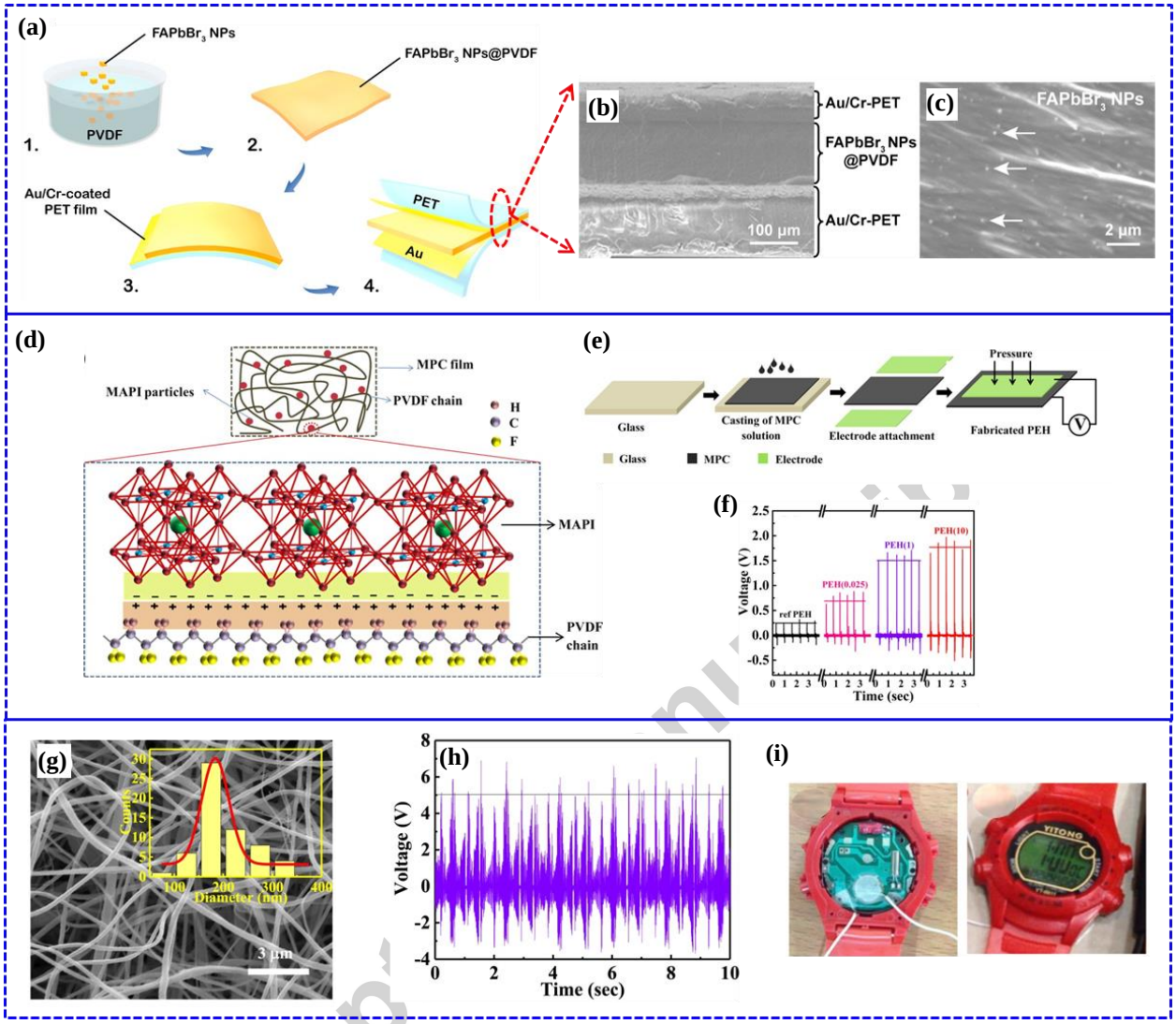

Fig.11 **Venkatraju et al.**

Accepted Manuscript

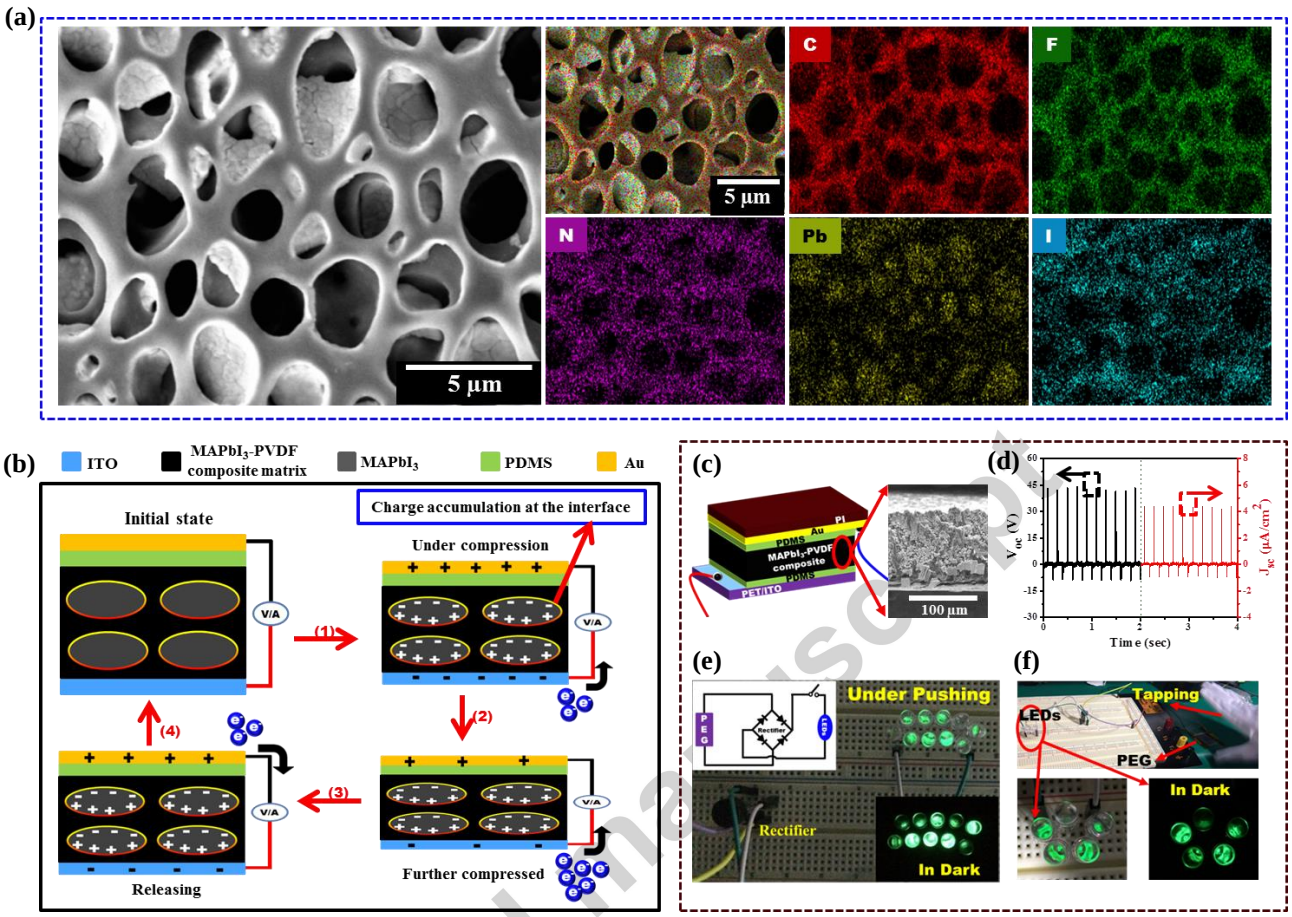

Fig.12 **Venkatraju et al.**

Accepted manuscript

ACCEPTED MANUSCRIPT

Highlights

- This study reviews recent progress of flexible piezoelectric generators based on OMHPs.
- Dielectric, ferroelectric and piezoelectric properties of OMHPs are discussed in detail.
- The advantages of OMHPs towards mechanical energy harvesting are discussed.
- The perspectives for the future development of OMHP-based nanogenerators are addressed.

Accepted manuscript